Published in final edited form as:

Free Radic Res. 2020 October ; 54(10): 695–721. doi:10.1080/10715762.2020.1836368.

Mechanistic computational modeling of the kinetics and regulation of NADPH oxidase 2 assembly and activation facilitating superoxide production

Shima Sadri[#a], **Namrata Tomar**[#a], **Chun Yang**[b], **Said H. Audi**[c], **Allen W. Cowley**[b], **Ranjan K. Dash**[a,b]

[a]Department of Biomedical Engineering, Medical College of Wisconsin, Milwaukee, WIS, USA;

[b]Department of Physiology, Medical College of Wisconsin, Milwaukee, WIS, USA;

[c]Department of Biomedical Engineering, Marquette University, Milwaukee, WIS, USA

[#] These authors contributed equally to this work.

Abstract

Reactive oxygen species (ROS) play a crucial role in many physiological processes. However, ROS overproduction leads to oxidative stress, which plays a critical role in cell injury/death and the pathogenesis of many diseases. Members of NADPH oxidase (NOX) family, most of which are comprised of membrane and cytosolic components, are known to be the major nonmitochondrial sources of ROS in many cells. NOX2 is a widely-expressed and well-studied NOX family member, which is activated upon assembly of its membrane subunits gp91^{phox} and p22^{phox} with its cytosolic subunits p40^{phox}, p47^{phox}, p67^{phox}, and Rac, facilitating ROS production. NOX2 activation is also enhanced by GTP and inhibited by GDP. However, there remains a lack of a mechanistic, quantitative, and integrated understanding of the kinetics and regulation of the assembly of these subunits and their relative contributions toward NOX2 activation and ROS production. Toward this end, we have developed a mechanistic computational model, which incorporates a generalized random rapid equilibrium binding mechanism for NOX2 assembly and activation as well as regulations by GTP (activation), GDP (inhibition), and individual subunits enhancing the binding of other subunits (mutual binding enhancement). The resulting model replicates diverse published kinetic data, including subunit concentration-dependent NOX2 activation and ROS production, under different assay conditions, with appropriate estimates of the unknown model parameters. The model provides a mechanistic, quantitative, and integrated framework for investigating the critical roles of NOX2 subunits in NOX2 assembly and activation facilitating ROS production in a variety of physiological and pathophysiological conditions. However, there is also a need for better quantitative kinetic data based on current understanding of NOX2 assembly and activation in order to test and further develop this model.

✉**CONTACT** Ranjan K. Dash rdash@mcw.edu Departments of Biomedical Engineering and Physiology, Medical College of Wisconsin, 8701 Watertown Plank Road, Milwaukee, WI-53226, USA.

Disclosure statement

No potential conflict of interest was reported by the author(s).

Keywords

Phagocyte oxidase; cell membrane oxidase; NOX2 assembly and activation; reactive oxygen species production; enzyme kinetics

Introduction

Reactive oxygen species (ROS), such as superoxide ($O_2^{\cdot -}$) and hydrogen peroxide (H_2O_2), are produced in cells from partial reduction of O_2 through several processes; for example, mitochondrial respiration [1–3], enzymatic reactions of xanthine oxidase (XO) [4–6] and NADPH oxidase (NOX) [7–12], or interactions with xenobiotic compounds [13]. ROS plays an important role in various physiological functions, including innate immunity, regulation of redox-dependent cell signaling cascades, cell proliferation and differentiation, and production of hormones [13–19]. Oxidative stress refers to imbalance between pro- and anti-oxidant processes due to either excess ROS production or deficiency in antioxidants capacity, which leads to macromolecular (e.g. DNA, proteins, lipids) damage and cell injury/death, ultimately leading to various diseases [1–3,13,19].

Members of NOX family, most of which are comprised of membrane and cytosolic proteins, are known to be the major nonmitochondrial sources of ROS in various tissues/cells [7–12]. Different NOX complexes are formed and activated on the cell membrane in response to different stimulatory signals (e.g. growth factors, cytokines, Ca^{2+}). ROS production, which is the primary result of the catalytic function of an assembled and activated NOX complex, varies between cell types. This property of NOX family is very different from other ROS generating systems for which ROS are byproducts of their usual physiological function (e.g. mitochondria). The physiological function of NOXs (*via* ROS production) includes regulation of cell signaling, gene expression, cell growth and division, and host cell defense among others [10,12,14–18,20]. NOX deficiencies/defects have been linked to immunosuppression, hypothyroidism, and chronic granulomatous disease [15,21,22]. There is also ample evidence that excess ROS generated by NOXs play a critical role in the pathogenesis of many chronic diseases, such as atherosclerosis, heart disease, lung disease, kidney disease, hypertension, diabetes, aging, neurodegeneration, and cancer [10,12,13,23–28].

Seven NOX family members (NOX1–5 and DUOX1–2) have been identified. The membrane components of each consist of at least six transmembrane α-helixes, two iron-heme groups, an FAD molecule, and an NADPH-binding domain [7–12,26]. The NOX family members differ in their membrane and cytosolic components, modes of activation, and reaction products. For example, activated NOX1–3 and NOX5 mainly produce $O_2^{\cdot -}$, while activated NOX4 and DUOX1–2 mainly produce H_2O_2 [10–12,29]. NOXs have been found in fungi, plants, invertebrates, and in multiple tissues/organs in mammals [10–12,30]. Among these, NOX1 is highly expressed in the colon [26], NOX3 is highly expressed in the inner ear [31], and NOX4 and NOX5 are highly expressed in the kidney and blood vessels and have been implicated in the regulation of blood pressure [27,32–35].

NOX2, originally discovered in neutrophils and other phagocytes, is a widely-expressed, highly orchestrated, and well-studied NOX family member [7–12]. NOX2 plays a key role in autoimmunity and malignancy [36], as demonstrated by the reduction of lung metastases in NOX2-deficient mice [37]. Deficiency in some key components of NOX2 is also known to lead to a rare genetic disorder, namely the chronic granulomatous disease [22,38,39]. Several early studies on NOX2-activated $O_2^{\cdot -}$ production were carried out by Pick and colleagues in cell-free systems, stimulated through unsaturated fatty acids and sodium dodecyl sulfate (SDS) [40,41]. In addition, exogenous FAD-dependent NOX2 activation and $O_2^{\cdot -}$ production was shown to occur through relipidated cytochrome b_{558} (Cytb_{558}) in the absence of NOX2 cytosolic components, demonstrating that membrane flavocytochrome b_{558} (Flavocytb_{558}) alone is sufficient to produce $O_2^{\cdot -}$ as it comprises the electron transport apparatus of NOX2 [42,43]. Subsequently, the kinetic features of NOX2 assembly and activation *in vitro* using purified relipidated and reflavinated Cytb_{558} and recombinant cytosolic components activated by lithium dodecyl sulfate (LDS) were also demonstrated [44]. Though several aspects of NOX2 assembly and activation differ between cell-based and cell-free systems (e.g. distinct roles of cytosolic subunits p47^{phox} and p67^{phox} [44–49]; distinct mechanisms of activation (see below)), due to its enormous simplicity and ease of manipulation, the cell-free systems have been extensively used to study different aspects of NOX2 assembly and activation.

The components of NOX2 complex include two transmembrane proteins gp91^{phox} (also known as Nox2 protein) and p22^{phox} and four cytosolic proteins p40^{phox}, p47^{phox}, p67^{phox}, and small GTPase Rac1/2 (Figure 1(A,B); *phox* refers to phagocyte oxidase). Activation of NOX2 requires the binding of phosphorylated/activated cytosolic subunits p47^{phox} and p67^{phox} or the p47^{phox}.p67^{phox} complex as well as Rac-GTP (active) to the membrane subunits complex gp91^{phox}.p22^{phox}, which constitutes Flavocytb_{558} (Figure 1(B)) [38,44,45,48–55]. In addition, p40^{phox} is shown to be required for NOX2 activation in phagosomes [55–57]. The activated NOX2 complex mediates the transfer of electrons from the substrate NADPH to molecular O_2 resulting in $O_2^{\cdot -}$ production through its catalytic action. The activated NOX2 complex is also shown to be highly specific to NADPH, responding poorly to NADH [58]. Each of the cytosolic subunits contributes towards NOX2 activation to varying extents, depending on the concentrations of these subunits and the concentrations of guanine nucleotides (GTP and GDP) [46,47,59–64]. NOX2 activation in cell-free assays was found to be enhanced by GTP and inhibited by GDP [59,60]. The regulation of NOX2 activation by GTP and GDP in cell-based assays has been attributed to the dissociation of Rac-GDP from the RhoGDI-RacGDP complex and the exchange of GTP for GDP on Rac (resulting in Rac activation) involving the complex Rho/Rac GTPase regulation cycle [14,65–70].

During NOX2 activation, p22^{phox} forms a mutually stabilising complex with gp91^{phox} on the cell membrane, with its carbonyl terminus enabling the binding of phosphorylated/activated cytosolic subunit p47^{phox} [38,52–55]. Concomitantly, the phosphorylated/activated cytosolic subunit p67^{phox} and Rac in GTP-bound form (active) attach directly to gp91^{phox} of Flavocytb_{558} [48, 49, 53, 54, 70]. The binding of p67^{phox} in combination with Rac and other

cytosolic subunits (p47^{phox} and/or p40^{phox}) to Flavocytb_{558} makes the complex to transfer electrons at a significant rate. It has also been shown that the subunit p47^{phox} is required for the electron transfer to proceed beyond the flavin center to heme site in Flavocytb_{558} and then to molecular O_2 for $O_2^{\cdot -}$ production [46,47,63]. Furthermore, p40^{phox} has been shown to enhance the binding of p47^{phox} to p22^{phox}, thereby enhancing NOX2 activation and $O_2^{\cdot -}$ production [64]. It has also been shown that the binding of p47^{phox} to p22^{phox} influences the binding of p67^{phox} to gp91^{phox} and *vice versa*, based on which the so-called "mutual binding enhancement hypothesis" was proposed [61]. Some of these cell-free studies have provided us the key kinetic data required for the development of the present computational model. The data utilized in this model also include the evidence that NOX2 activity is enhanced by micromolar [GTP] and reduced by millimolar [GDP] [59,60], and the data showing that Rac in GTP-bound form (active) can translocate and bind to Flavocytb_{558} independent of other NOX2 cytosolic subunits [50,51], thereby enhancing the binding of p67^{phox} [62].

Despite a considerable number of biochemical studies regarding NOX2 assembly and activation, there is a lack of a mechanistic and quantitative understanding of the kinetics and regulation of the assembly of NOX2 subunits and their relative contributions toward the oxidase activation and $O_2^{\cdot -}$ generation. Moreover, although experimental studies have considered the contributions of various cytosolic subunits and the effects of various regulators (e.g. GTP and GDP), NOX2 kinetics have not been considered from an integrated prospective, which enables the development of quantitative hypotheses. We therefore recently developed a thermodynamically constrained computational model [71] that provides the kinetics and regulation of the NOX2 complex-mediated electron transfer and $O_2^{\cdot -}$ production upon its assembly and activation. The model was developed using multiple published datasets describing NOX2 kinetics in different assay systems [58,72–77]. However, the kinetics and regulation of the different cytosolic subunit concentration-dependent NOX2 assembly and activation facilitating $O_2^{\cdot -}$ production were not considered in that study [71].

The objective of the present study was therefore to develop a mechanistic computational model of NOX2 assembly and activation facilitating $O_2^{\cdot -}$ production. The model is based on a generalized random rapid equilibrium binding mechanism for the binding of cytosolic p40^{phox}, p47^{phox}, p67^{phox}, and Rac to the membrane gp91^{phox}. p22^{phox} complex (Flavocytb_{558}) toward NOX2 assembly and activation. It also includes the regulation of NOX2 assembly and activation by guanine nucleotides (GTP and GDP) and individual subunits enhancing the binding of other subunits (i.e. mutual binding enhancement hypothesis). This model provides the first quantitative and integrated understanding of the kinetics and regulation of NOX2 assembly and activation facilitating $O_2^{\cdot -}$ production in diverse experimental preparations from different groups. In addition, it provides a mechanistic and quantitative framework for investigating the critical role of NOX2 in $O_2^{\cdot -}$ production, which plays a key role in the regulation of diverse cellular mechanisms in health and disease.

Materials and methods

Proposed kinetic mechanism for NOX2 assembly and activation facilitating superoxide production

Upon assembly and activation (Figure 1(B)), the NOX2 complex catalyzes the production of two molecules of $O_2^{\cdot -}$ by transferring two electrons from NADPH to two molecules of O_2 through different redox centers of gp91^{phox}.p22^{phox} or Flavocytb_{558} (i.e. FAD and heme/Cytb_{558}) [71]:

$$NADPH + 2O_2 \leftrightarrow NADP^+ + 2O_2^{\cdot -} + H^+ \quad (1)$$

In contrast, the resting NOX2 (unassembled and inactivated; Figure 1(A)) does not enable electrons transfer from NADPH to the flavin center or beyond at a significant rate, as shown by the absence of a significant reduction of flavin or heme site of Flavocytb_{558} [46,47,63]. Under this scenario, the gp91^{phox} and p22^{phox} subunits co-stabilize one another on the cell membrane, while the cytosolic subunits p40^{phox}, p47^{phox} and p67^{phox} exist in inactive (unphosphorylated) forms and Rac exists in GDP-bound (inactive) form. Upon stimulation, there is an exchange of GDP for GTP leading to Rac activation (Rac becomes GTP-bound) and its translocation to the cell membrane and its interaction with the gp91^{phox}.p22^{phox} complex [14,50,51,65–70]. Concomitant phosphorylation of the subunits p47^{phox} and p67^{phox} by protein kinases leads to their activation, allowing their translocation and interactions with the p22^{phox}.gp91^{phox} complex on the cell membrane [38,48,49,52–55]. This phosphorylation-translocation is one of the major events of the oxidase activation.

We assume that the binding of phosphorylated/activated cytosolic subunits p40^{phox}, p47^{phox}, p67^{phox} and Rac to the membrane gp91^{phox}.p22^{phox} complex (Flavocytb_{558}) occurs in a random order and rapid equilibrium manner with p40^{phox} not contributing significantly to the assembly and activation of NOX2 in the absence of p47^{phox}. These events are illustrated in Figure 2 with the membrane gp91^{phox}.p22^{phox} complex denoted as E. The K'_is (i = p47^{phox}, p67^{phox}, Rac) denote the apparent dissociation/binding constants for the cytosolic subunits rapid equilibrium binding reactions with the membrane subunits, as determined by the phosphorylation status of the cytosolic subunits and the levels of GTP and GDP. K'_is are the measures of the affinities of the cytosolic subunits for the membrane subunits, which depend on the particular experimental system (cell-free or cell-based) employed in a given study as well as the levels of GTP, GDP, p40^{phox}, p47^{phox}, p67^{phox}, and Rac.

Key experimental data characterizing the cytosolic subunit concentration-dependent NOX2 reaction flux

In order to identify the unknown model parameters characterizing the proposed kinetic mechanism, six sets of experimental data collected by four different groups are utilized. Two sets of these data are from Uhlinger et al. [60,61], who studied the effects of guanine nucleotides (GTP and GDP) and the binding of cytosolic subunits (p47^{phox} and p67^{phox}) to the membrane subunits complex gp91^{phox}.p22^{phox} (Flavocytb_{558}) on NOX2 activation and $O_2^{\cdot -}$ production. Uhlinger et al. [60] used a semi-recombinant cell-free NOX2 activation

system (i.e. that included isolated plasma membrane with recombinant cytosolic components) to investigate the activating role of GTP and inhibiting role of GDP on $p47^{phox}$ and $p67^{phox}$ (no $p40^{phox}$ and Rac) dependent NOX2 assembly, activation, and $O_2^{\cdot -}$ production. In another study, the same group used a similar enzyme activation system to investigate the effects of $p47^{phox}$ and $p67^{phox}$ on one another's binding to Flavocytb_{558} to activate NOX2 and produce $O_2^{\cdot -}$ (no $p40^{phox}$; 2 μM Rac; 10 μM GTP) [61]. Another set of data utilized for parameter identification is from Peveri et al. [59], who studied the enhancing effect of GTP on NOX2 activity in a similar cell-free system (no $p40^{phox}$ and Rac) to determine $O_2^{\cdot -}$ production as a function of GTP concentration. The fourth set of data utilized for parameter identification is from Nisimoto et al. [62], who used a cell-free system similar to that used by Peveri et al. [59] to investigate the effects of $p67^{phox}$ and Rac on one another's binding with Flavocytb_{558} to activate NOX2 and produce $O_2^{\cdot -}$ (no $p40^{phox}$ and $p47^{phox}$; 10 μM GTP).

Additional two sets of data utilized for parameter identification were collected by Cross et al. [63,64]. They studied the effects of the binding of cytosolic subunits $p40^{phox}$, $p47^{phox}$, $p67^{phox}$, and Rac to the membrane subunits $gp91^{phox}$ and $p22^{phox}$ on NOX2 activity, $O_2^{\cdot -}$ production, and regulation of $p47^{phox}$ binding affinity by $p40^{phox}$. Cross et al. used fully recombinant cell-free systems to determine Flavocytb_{558} and cytosolic subunit concentration-dependent NOX2 activation and $O_2^{\cdot -}$ production, and their regulations through $p40^{phox}$–$p47^{phox}$ interactions in the presence of saturating concentrations of GTP, NADPH and O_2. In one study, $p47^{phox}$, $p67^{phox}$ and Rac concentration-dependent NOX2 activity and $O_2^{\cdot -}$ production were assessed by varying one subunit concentration while maintaining the other two subunits concentrations at their saturating levels and doubling the concentration of Flavocytb_{558} [63]. In another study, the role of $p40^{phox}$ in NOX2 activation was evaluated in the presence and absence of $p47^{phox}$, which showed that $p40^{phox}$ contributes very little towards NOX2 activation in the absence of $p47^{phox}$. However, $p40^{phox}$ did enhance the binding of $p47^{phox}$ to $p22^{phox}$, thereby increasing NOX2 activity and $O_2^{\cdot -}$ production [64].

Computational model describing NOX2 reaction flux

Based on our postulated generalized random rapid equilibrium binding mechanism for NOX2 assembly and activation in Figure 2, and the detailed derivation described in Appendix A, NOX2 reaction flux at saturating concentrations of NADPH and O_2 is described by Equation 2:

$$J_{NOX2} = k_{NOX2} C_{Etot} \left(\frac{C_{p47}}{K'_{p47} + C_{p47}} \right) \left(\frac{C_{p67}}{K'_{p67} + C_{p67}} \right) \left(\frac{C_{Rac}}{K'_{Rac} + C_{Rac}} \right) \quad (2)$$

where $C_{Etot} = C_{\text{Flavocytb558}}$ denotes the total Flavocytb_{558} concentration; k_{NOX2} denotes NOX2 catalytic constant; C_{p47}, C_{p67} and C_{Rac} denote the concentrations of $p47^{phox}$, $p67^{phox}$ and Rac, respectively; K'_{p47}, K'_{p67} and K'_{Rac} denote the apparent binding constants for $p47^{phox}$, $p67^{phox}$ and Rac, respectively. The superscript "*phox*" is eliminated from the

equation for simplicity. It should be noted here that at limiting concentrations of the substrates NADPH and O_2, the NOX2 catalytic constant k_{NOX2} is a function of [NADPH] and [O_2], as shown in our recent publication [71]. More details on the derivation of NOX2 reaction flux can be found in Appendix A. We note here that, in our model formulation (Figure 2), $p40^{phox}$ is not essential for NOX2 assembly and activation, and hence it does not appear in Equation (2), which is valid for the plasma membrane.

As noted in the description of the experimental data from Uhlinger et al. [61], the binding of $p47^{phox}$ to Flavocytb_{558} influences the binding of $p67^{phox}$ to Flavocytb_{558} and vice-versa, indicating a regulatory role of $p47^{phox}$ on $p67^{phox}$ binding and *vice versa* (mutual binding enhancement). In addition, based on the data from Nisimoto et al. [62], the binding of $p67^{phox}$ to Flavocytb_{558} influences the binding of Rac to Flavocytb_{558} and vice-versa, suggesting a regulatory role of $p67^{phox}$ on Rac binding and *vice versa* (mutual binding enhancement). Based on our generalized model formulation, the same mutual binding enhancement also exists between $p47^{phox}$ and Rac, indicating a regulatory role of $p47^{phox}$ on Rac binding and *vice versa*. Based on the data of Cross et al. [64], $p40^{phox}$ enhances the binding of $p47^{phox}$ increasing NOX2 activity and $O_2^{\cdot -}$ production, whose effect is accounted for in our model *via* K'_{p47} in Equation 3(a) below. Moreover, NOX2 activity is enhanced by micromolar of GTP and attenuated by millimolar of GDP [59,60]. For the sake of generality in our model formulation, we also postulate that Rac binding to Flavocytb_{558} enhances the binding of $p47^{phox}$ and $p67^{phox}$ to Flavocytb_{558}. The apparent binding constants K'_{p47}, K'_{p67} and K'_{Rac} can then be phenomenologically expressed based on the standard Michaelis–Menten kinetic formulation for activations and inhibitions as follows:

$$K'_{p47} = K_{p47}\left(\frac{C_{GTP}^{nT}}{K_{GTP}^{nT}+C_{GTP}^{nT}}\right)\left(\frac{K_{GDP}^{nD}}{K_{GDP}^{nD}+C_{GDP}^{nD}}\right)\left(\frac{C_{p67}}{K''_{p67p47}+C_{p67}}\right)\left(\frac{C_{Rac}}{K''_{Racp47}+C_{Rac}}\right)\left(1+\frac{2C_{p40}}{K''_{p40}+C_{p40}}\right) \tag{3a}$$

$$K'_{p67} = K_{p67}\left(\frac{C_{GTP}^{nT}}{K_{GTP}^{nT}+C_{GTP}^{nT}}\right)\left(\frac{K_{GDP}^{nD}}{K_{GDP}^{nD}+C_{GDP}^{nD}}\right)\left(\frac{C_{p47}}{K''_{p47p67}+C_{p47}}\right)\left(\frac{C_{Rac}}{K''_{Racp67}+C_{Rac}}\right) \tag{3b}$$

$$K'_{Rac} = K_{\mathrm{Rac}}\left(\frac{C_{GTP}^{nT}}{K_{GTP}^{nT}+C_{GTP}^{nT}}\right)\left(\frac{K_{GDP}^{nD}}{K_{GDP}^{nD}+C_{GDP}^{nD}}\right)\left(\frac{C_{p67}}{K''_{p67Rac}+C_{p67}}\right)\left(\frac{C_{p47}}{K''_{p47Rac}+C_{p47}}\right) \tag{3c}$$

where C_{GTP} and C_{GDP} denote the concentrations of GTP and GDP, respectively; K_{GTP} and K_{GDP} denote the regulatory constants for GTP and GDP to enhance and inhibit NOX2 activity, respectively; nT and nD are the corresponding Hill coefficients; K''_{p47p67} and K''_{p47Rac} are the regulatory constants for $p47^{phox}$ to enhance the binding of $p67^{phox}$ and Rac, respectively; K''_{p67p47} and K''_{p67Rac} are the regulatory constants for $p67^{phox}$ to enhance the

binding of p47^{phox} and Rac, respectively; K''_{Racp47} and K''_{Racp67} are the regulatory constants for Rac to enhance the binding of p47^{phox} and p67^{phox}, respectively; and K''_{p40} is the regulatory constant for p40^{phox} to enhance the binding of p47^{phox}. The regulatory effect of p40^{phox} can be simply eliminated by substituting $C_{p40} = 0$ or by significantly increasing the value of K''_{p40} in Equation 3(a).

A Hill coefficient (nH) characterizes the cooperative binding of a ligand to a macromolecule. Although cooperativity often enhances the binding (positive cooperativity; $nH > 1$), it can also decrease the binding (negative cooperativity; $nH < 1$) or show no effect ($nH = 1$). The Hill coefficients nT and nD are incorporated into our model for simulating the guanine nucleotides-dependent regulations (i.e. enhancement by GTP and inhibition by GDP) of NOX2 activity observed in the studies of Uhlinger et al. [60] and Peveri et al. [59] (no Rac; no GTP-GDP exchange on Rac).

Model simplification

The model can be further simplified in terms of the number of unknown parameters by assuming the same extent regulatory effects of the individual cytosolic subunits with the other cytosolic subunits by applying the following constraints:

$$K''_{p47p67} = K''_{p47Rac} = K''_{p47} \tag{4a}$$

$$K''_{p67p47} = K''_{p67Rac} = K''_{p67} \tag{4b}$$

$$K''_{Racp47} = K''_{Racp67} = K''_{Rac} \tag{4c}$$

Here, we have assumed that p47^{phox} binding to the membrane subunits enhances p67^{phox} binding to the same extent as Rac binding (Equation (4a)); p67^{phox} binding to the membrane subunits enhances p47^{phox} binding to the same extent as Rac binding (Equation (4b)); and Rac binding to the membrane subunits enhances p47^{phox} binding to the same extent as p67^{phox} binding (Equation (4c)). These constraints reduce the number of unknown parameters by three, but a key question is whether such parameter reduction affords a good fit of the model solution to the available data. To test this, we have characterised three nested models (Models 1, 2 and 3; see Appendix B), based on the number of unknown parameters. Model 3 corresponds to Equations (2) and (3) without any parameter constraint; Model 2 corresponds to Equations (2) and (3)) with the parameter constraint of Equation (4); and Model 3 corresponds to Equations (2) and (3) with the parameter constraint of Equation (4) and with $K''_{p47} = 0$, $K''_{p67} = 0$, and $K''_{Rac} = 0$.

Numerical estimation of NOX2 model parameters

Each of the kinetic models developed for NOX2 assembly and activation facilitating $O_2^{\cdot -}$ production contains several unknown parameters. The number of unknown parameters depends on the complexity of a particular model. As described above, Model 3 has 12 unknown parameters, Model 2 has 9 unknown parameters, and Model 1 has 6 unknown

parameters. The parameter estimation for these three models entailed a combined use of all the available experimental data related to NOX2 subunits assembly, activation, and $O_2^{\cdot -}$ production [59–64] and minimizing the sum of squared differences error function (Equation (5)) for fitting the model solutions to these experimental data:

$$\min_{\phi} E(\phi),\ E(\phi) = \sum_{k=1}^{N_{\exp}} \frac{1}{N_{data,k}} \left(\sum_{j=1}^{N_{\text{data},k}} \left(\frac{J_{j,k}^{data} - J_{j,k}^{\text{model}}(\phi)}{\max\left(J_{j,k}^{data}\right)} \right)^2 \right) \quad (5)$$

where N_{exp} is the number of experiments; $N_{data,k}$ is the number of data points in the k^{th} experiment; $J_{j,k}^{data}$ are the experimental data; and $J_{j,k}^{\text{model}}(\phi)$ are the corresponding model solutions that depend on the values of the model parameters ϕ. The accuracy in the estimated model parameters values and the robustness of the model fits to the experimental data are assessed based on the value of the sum of squared differences error function $E(\phi)$ and statistical modelling criteria. Our approach for parameter estimation and testing the robostness of the model fits are detailed in Appendix B.

Results

The parameterization results of the three competing models of NOX2 assembly and activation showed that Model 3 with 12 unknown parameters resulted in the least sum of squared differences of 3.01 and the best fit to the available data. Therefore, Model 3 was considered as the best model of NOX2 assembly and activation, and the estimated parameter values and simulation results for Model 3 are presented in this section. In parametrizing the model, a hybrid Monte-Carlo and Fmincon approach in MATLAB was used as detailed in Appendix B. This resulted in parameter values shown in Table 1 for which Model 3 solution best fits the kinetic data of Cross et al. [63,64] as shown in Figure 3, and parameter values in Table 2 for which Model 3 solution best fits the kinetic data of Uhlinger et al. [60,61], Peveri et al. [59], and Nisimoto et al. [62] as shown in Figures 4 and 5. Model 3 was also used to predict other kinetic data shown in Figures 6 and 7 that were not used for model parameterization in addition to Figure 8 to corroborate the model and estimated parameter values. In what follows, all the simulation results were generated using Model 3 using the parameters values in Tables 1 and 2.

Cytosolic subunit concentration-dependent effects on NOX2 activity and the regulatory effect of $p40^{phox}$ on $p47^{phox}$ binding based on the kinetic data of Cross et al. [63,64]

As shown in Figure 3, using the estimated model parameter values in Table 1 (Model 3 = Model 2 = Model 1), we were able to simulate very well the concentration-dependent effects of Flavocytb_{558}, $p40^{phox}$, $p47^{phox}$, $p67^{phox}$ and Rac on NOX2 activity and the regulatory effects of $p40^{phox}$ on $p47^{phox}$ binding to Flavocytb_{558} in activating NOX2 enzyme in cell-free systems.

Simulations of the effect of $p40^{phox}$ on NOX2 activity for varying concentrations of $p47^{phox}$ and high (saturating) concentrations of $p67^{phox}$ and Rac are shown in Figure 3(A–C). The effect of $p47^{phox}$ at high concentrations of $p67^{phox}$ and Rac, the effect of $p67^{phox}$ at high concentrations of $p47^{phox}$ and Rac, and the effect of Rac at high concentrations of $p47^{phox}$

and p67^{phox} in the absence and presence of high concentrations of p40^{phox} are simulated in Figure 3(D–F). In these simulations, Flavocytb_{558} concentration was fixed at 0.3 pmol/well, as per the experimental protocol. Cross et al. [64] used a cell-free system to demonstrate the role of p40^{phox} on NOX2 activity and found NOX2 activity to be very weak in the absence of p47^{phox}. Addition of p47^{phox} increases NOX2 activity by several hundred-fold and this enhancement could not be explained by just the additive effects of p40^{phox} and p47^{phox}. From this analysis, it was concluded that p40^{phox} functions by mainly increasing the binding affinity of p47^{phox} for Flavocytb_{558}, thereby enhancing NOX2 activity.

Our model simulated very well the concentration-dependent effect of p40^{phox} on NOX2 activity with very low enzyme activity in the presence of only p40^{phox} (Figure 3(A)) and high enzyme activity in the presence of both p40^{phox} and p47^{phox} (Figure 3(B,C)). Model simulations also showed that p40^{phox} does not act additively with p47^{phox}, p67^{phox} and Rac to enhance NOX2 activity, as depicted in Figure 3(D–F), and that the enhanced effect is achieved primarily by increasing the binding affinity of p47^{phox} for Flavocytb_{558} by p40^{phox} (Equation 3(a)). In addition, the effect of varying the concentration of Flavocytb_{558} on NOX2 activity [63] was simulated very well as shown in Figure 3(G–I). Flavocytb_{558} increased NOX2 activity in a linear concentration-dependent fashion, as observed experimentally, when the assay medium contained various concentrations of the subunits p47^{phox}, p67^{phox} and Rac at any level of p40^{phox}. The model also fits quite well the Cross et al. [63] experimental data (Figure 3(G–I)), for which the concentrations of p47^{phox}, p67^{phox} and Rac were varied one at a time over a range of Flavocytb_{558} concentrations, while keeping the concentrations of other subunits fixed at maximal levels.

Regulatory effects of guanine nucleotides on NOX2 assembly, activation, and superoxide generation based on the kinetic data of Uhlinger et al. [60] and Peveri et al. [59]

As demonstrated in Figure 4, using the estimated model parameter values in Table 2 (Model 3), we were able to simulate very well the regulatory effects of GTP and GDP on NOX2 assembly, activation, and $O_2^{\cdot -}$ production based on the experimental data of Uhlinger et al. [60] and Peveri et al. [59].

Uhlinger et al. [60] studied the regulatory roles of guanine nucleotides (GTP and GDP) on the cytosolic subunits (p47^{phox} and p67^{phox}) concentration-dependent NOX2 assembly, activation, and $O_2^{\cdot -}$ generation with a negligible Rac level (estimated to be ~0.02 μM) and saturated NADPH and O_2 levels in reconstituted cell-free systems (isolated membrane preparation). They demonstrated that 10 μM GTP maximally activated $O_2^{\cdot -}$ generation, while 10 mM GDP significantly inhibited $O_2^{\cdot -}$ generation, with appreciable baseline activity without any added GTP and GDP (due to partial activation of NOX2 enzyme by endogenously present GTP; basal activity). These kinetic data were used to model the cytosolic subunit concentration-dependent NOX2 assembly, activation, $O_2^{\cdot -}$ generation, and regulation by guanine nucleotides. As illustrated in Figures 4(A,B), the model nicely simulated the guanine nucleotide regulation of NOX2 activity with varying levels of p47^{phox} and p67^{phox}, as observed experimentally [60]. The effects of varying the levels of GTP and GDP with fixed levels of p47^{phox} and p67^{phox} (1.3 μM each) were then simulated at high

NADPH and O_2 levels and a baseline Rac level of ~0.02 μM to determine the opposing effects of guanine nucleotides on NOX2 activity. The stimulatory effect of GTP and the reciprocal inhibitory effect of GDP are illustrated in Figures 4(C,D), and are compared to the available experimental data on the inhibitory effect of GDP in the presence of 10 μM GTP [60] and the stimulatory effect of GTP in the absence of GDP [59] (dark blue lines in Figure 4(C,D)). The model predicted the GTP and GDP-induced alterations in the binding constants for the subunits p47*phox* and p67*phox*. Importantly, these model analyses suggest that the oxidase-associated GTP and GDP levels are likely to participate in NOX2 complex formation.

Regulatory effects of mutual binding enhancements between cytosolic subunits on NOX2 assembly, activation, and superoxide generation based on the kinetic data of Uhlinger et al. [61] and Nisimoto et al. [62]

As demonstrated in Figure 5, using the estimated model parameter values from Table 2 (Model 3), we were able to simulate very well the regulatory controls of NOX2 assembly, activation, and $O_2^{\cdot -}$ production *via* mutual binding enhancements between the cytosolic subunits p47phox, p67phox and Rac based on the experimental data of Uhlinger et al. [61] and Nisimoto et al. [62]. Figure 5(A,B) is based on the study by Uhlinger et al. [61] in which a reconstituted cell-free system was used to determine the influence of NOX2 subunits p47*phox* and p67*phox* upon each other's binding to Flavocytb_{558} for the oxidase activity, carried out in the presence of exogenously added 2 μM Rac and 10 μM GTP. Similarly, Figure 5(C,D) is based on the study by Nisimoto et al. [62] in which a similar cell-free system was utilized to determine the influence of NOX2 subunits p67*phox* and Rac upon each other's binding to Flavocytb_{558} for the oxidase activity, carried out in the presence of negligible p47phox (estimated to be ~0.01 μM) and 10 μM added GTP. Mutually enhanced binding of cytosolic subunits to Flavocytb_{558} required modification of our model by addition of regulatory mechanisms describing the kinetics of p47*phox* binding enhanced by p67*phox* and Rac *via* Equation 3(a), the kinetics of p67*phox* binding enhanced by p47*phox* and Rac *via* Equation 3(b), and the kinetics of Rac binding enhanced by p47*phox* and p67*phox* *via* Equation 3(c). This modified model suggests interdependent changes in the values of the apparent K_m and V_{max} values of NOX2 with respect to the cytosolic subunits.

As seen in Figure 5(A,B), the apparent K_m and V_{max} values for the subunit p47*phox* are modified at variable concentrations of the subunit p67*phox* and *vice versa*. In this case, the subunit Rac and GTP levels were held constant at 2.02 μM and 10.5 μM, in the presence of estimated basal concentration of 0.02 μM and 0.5 μM, respectively. Also, as seen in Figure 5(C,D), the apparent K_m and V_{max} values for the subunit Rac are modified at variable concentrations of the subunit p67*phox* and vice-versa. In this case, the subunit p47*phox* and GTP levels were held constant at 0.01 μM and 10.5 μM, with an estimated basal concentration of 0.01 μM and 0.5 μM, respectively. Experimentally [61,62], the rate of $O_2^{\cdot -}$ generation was measured at saturated NADPH and O_2 levels to ascertain its dependency on the varying concentrations of the subunit p47*phox* at various fixed concentrations of the subunit p67*phox* and vice-versa for Figure 5(A,B), and on the varying concentrations of the subunit Rac at various fixed concentrations of the subunit p67*phox* and *vice versa* for Figure

5(C,D). The model simulations found that as the concentration of either of the subunits decreases, the binding of the other subunits to Flavocytb_{558} becomes weaker such that at lower concentrations of these subunits, NOX2 reaction flux ($O_2^{\cdot -}$ production) decreases significantly.

Importantly, the model simulations of Figure 5 informed us about the mutual binding enhancements of cytosolic subunits on each other's bindings to Flavocytb_{558}, as evidenced by the studies of Uhlinger et al. [61] and Nisimoto et al. [62]. Based on Uhlinger et al. [60] data compared to Uhlinger et al. [61] data, the presence of the subunit Rac in the reaction mixture (2 μM added) resulted in significantly higher V_{max} values (20-fold increase) showing a key regulatory role of Rac in enhancing the binding of cytosolic subunits p47^{phox} and p67^{phox} to Flavocytb_{558} as well as in significantly higher active NOX2 complex formation. In addition, based on Equation (2), our model indicates that a basal concentration of the cytosolic subunits p47^{phox}, p67^{phox} and Rac are required for NOX2 assembly and activation. Thus, the proposed model provides a unified theory/hypothesis that quantitatively explains these diverse experimental datasets. We have also introduced Hill coefficients to model the cooperative regulation of NOX2 cytosolic subunits binding to Flavocytb_{558} by guanine nucleotides, i.e. GTP and GDP (see Equations (3a–c)).

Model corroboration showing the regulations of apparent NOX2 kinetic parameters by guanine nucleotides and cytosolic subunits

The regulatory effects of guanine nucleotides (GTP and GDP) and cytosolic subunits (p47^{phox}, p67^{phox}, and Rac) on the binding of p47^{phox}, p67^{phox}, and Rac to Flavocytb_{558} characterizing NOX2 assembly and activation were further analyzed by our model. We computed the apparent K_m and V_{max} values for p67^{phox} as a function of p47^{phox} for different concentrations of GTP, GDP, and Rac; the apparent K_m and V_{max} values for p47^{phox} as a function of p67^{phox} for different concentrations of GTP, GDP and Rac; and the apparent K_m and V_{max} values for Rac as a function of p67^{phox} for different concentrations of GTP, GDP and p47^{phox}. These calculations were made to study the regulatory effects of varying concentrations of GTP, GDP, and cytosolic subunits at saturated concentrations of NADPH and O_2 (experimental conditions exactly the same as that for Figures 4 and 5) on the apparent kinetic parameters governing the binding of cytosolic subunits to Flavocytb_{558}. These model simulation results are shown in Figures 6–8.

The apparent NOX2 kinetic parameters are calculated numerically by equating Equation (2) for J_{NOX2} with K'_is defined by Equations (3a–c) with an equation of the form $J_{NOX2} = V_{max,S}C_S/(K_{m,S}+C_S)$, where S stands for the subunits p47^{phox}, p67^{phox} or Rac, and C_S denotes the concentration of S. This way, the apparent $K_{m,S}$ and $V_{max,S}$ are functions of the other variables. For example, if S = p47^{phox}, the $K_{m,S}$ and $V_{max,S}$ are functions of p67^{phox}, GTP, GDP, and Rac at saturated levels of NADPH and O_2. In this case, the $V_{max,S}$ can be easily computed numerically by evaluating Equation (2) at very high C_S, and the $K_{m,S}$ can be easily computed numerically by solving the value of C_S at which the value of J_{NOX2} is equal to $V_{max,S}/2$ in Equation (2). We emphasize here that, for these computations, NOX2 model structure includes all the modular components, namely the subunits assembly,

guanine nucleotides regulation of the assembly, mutual binding enhancement, and $O_2^{\cdot -}$ production.

The results of these model predictions reveal that the apparent K_m of p67^{phox} (or p47^{phox} or Rac) was decreased, while the apparent V_{max} with respect to p67^{phox} (or p47^{phox} or Rac) was increased with increasing concentrations of the other subunit p47^{phox} (or p67^{phox} or Rac). The same was the case with increasing concentrations of GTP and decreasing concentrations of GDP. However, it is worth mentioning here that the apparent K_m of p47^{phox} did not decrease appreciably with increasing concentrations of Rac and apparent K_m of Rac did not decrease appreciably with increasing concentrations of p47^{phox} and p67^{phox} (Figures 7(E) and 8(E)). Decreased $K_{m,S}$ and increased $V_{max,S}$ indicate increased binding affinity of the cytosolic subunits p47^{phox}, p67^{phox}, and Rac for the membrane Flavocytb_{558} and increased overall NOX2 activity, respectively. Therefore, p47^{phox} appears to increase the binding affinity of p67^{phox} for Flavocytb_{558} and *vice versa*, albeit differentially, which is consistent with the mutual binding enhancement hypothesis, originally proposed by Uhlinger et al. [61]. Our model also predicts that there is no mutual binding enhancement between p47^{phox} and Rac, and only negligible enhancement in the binding of Rac by p67^{phox} (see Table 2).

An important observation from the simulations in Figures 6–8 is that $K_{m,p67}$ is an order of magnitude higher than $K_{m,p47}$ and $K_{m,Rac}$, while $V_{max,p67}$, $V_{max,p47}$, and $V_{max,Rac}$ are of the same order of magnitude. This indicates that p47^{phox} enhances the binding affinity of p67^{phox} (reduces $K_{m,p67}$) 10 times more than p67^{phox} enhances the binding affinity of p47^{phox} and Rac (reduces $K_{m,p47}$ and $K_{m,Rac}$) for Flavocytb_{558}. Furthermore, our model predictions show that GTP increases the binding affinities of p47^{phox}, p67^{phox}, and Rac for Flavocytb_{558}, while GDP decreases the binding affinities of these subunits for Flavocytb_{558}. Interestingly, our model predictions also show that there is no enhancement in the binding affinity of Rac for Flavocytb_{558} by p47^{phox} and p67^{phox} (K''_{p67Rac} = 0.009 and K''_{p47Rac} = 0.003; Table 2), and there is negligible enhancement in the binding affinity of p47^{phox} for Flavocytb_{558} by Rac (K''_{Racp47} = 0.05; Table 2). The assembly and activation of NOX2 is seen to be maximal at 10 μM GTP, 0 mM GDP, and 2 μM Rac at which the apparent $K_{m,S}$ is minimal and the apparent $V_{max,S}$ is maximal. The model predictions in Figures 6 and 7 match well with the measured data from the experiments by Uhlinger et al. [61]. It is important to recognize that since these experimental data were not used for model parameterization, the ability of the model to predict these data provides additional support for its accuracy and utility. Also, the model predictions in Figure 8 provide a good insight into the behavior of the apparent K_m and V_{max} of Rac with respect to varying concentrations of p67^{phox} for various concentrations of GTP, GDP, and p47^{phox}.

Discussion

The goal of the present study was to develop a simple, yet adequately detailed, computational model of NOX2 assembly and activation on the cell membrane that can provide a mechanistic and quantitative understanding of the kinetics and regulation of the assembly of NOX2 subunits and their relative contributions to NOX2 activation and $O_2^{\cdot -}$

production. In view of the enormous complexity of the biological process of NOX2 assembly and activation, several assumptions were required to simplify the process in developing this model. The major assumption was that the assembly and activation of NOX2 occurs through random rapid equilibrium binding of its cytosolic subunits ($p40^{phox}$, $p47^{phox}$, $p67^{phox}$, and Rac) with its membrane subunits ($gp91^{phox}$ and $p22^{phox}$). This is further activated by GTP and inhibited by GDP and further regulated by the mutual binding enhancement mechanism, consistent with the existing literature [59–62]. The complexity of the model and the hypotheses was systematically incorporated through a modular model building and hypothesis testing approach. The model was rigorously parameterized and challenged using diverse experimental data obtained under different assay conditions [59–64], which then provided reliable and predictive representations of NOX2 assembly and activation. The ability of the model to simulate quite well a diverse spectrum of experimental data from various laboratories suggest that the underlying assumptions are reasonable. It should be emphasized that a model cannot describe experimental data from diverse sources under different assay conditions with suitable model parameter values unless appropriate kinetic mechanisms are incorporated no matter how many unknown parameters it contains, as rigorously tested in Appendix B. The model as developed represents a first step toward a quantitative and integrated understanding of several aspects of NOX2 assembly and activation, specifically how different cytosolic components ($p40^{phox}$, $p47^{phox}$, $p67^{phox}$, and Rac) and guanine nucleotides (GTP and GDP) regulate the overall process. Consistent with the process of model building, more details of the protein–protein interactions, phosphorylation and dephosphorylation, alternative NOX2 assembly and activation mechanisms, and the regulation of the assembly and activation process by the Rho/Rac GTPase regulation cycle can be integrated into future iterations of this model as appropriate quantitative data becomes available.

The kinetic data used to develop and parameterize the model was obtained from studies by different groups in which the experiments were carried out under different assay conditions [59–64]. For example, Uhlinger et al. [60] did not initially include Rac in their studies, but rather they studied the activating effects of GTP and inhibitory effects of GDP on the overall NOX2 activity ($O_2^{\cdot -}$ production), while varying the levels of the cytosolic subunits $p47^{phox}$ and $p67^{phox}$. However, in a subsequent study [61], they added Rac (2 μM) to the reaction mixture with saturating level of GTP (10 μM), and thereby, they observed the mutual binding enhancements of $p47^{phox}$ and $p67^{phox}$ for Flavocytb_{558}. Importantly, there was a 20-fold increase in the overall NOX2 activity with the addition of 2 μM Rac as a consequence of enhanced NOX2 complex formation on the cell membrane. These data were nicely recapitulated with our computational model as well as the GTP- and GDP-dependent kinetic data from Uhlinger et al. [60] and the GTP-dependent kinetic data from Peveri et al. [59]. Importantly, the model was also able to reproduce the kinetic data from an independent study by Nisimoto et al. [62], thereby further validating the predictive value of the model and also testing the mutual binding enhancements hypothesis (i.e. $p67^{phox}$ and Rac enhancing the binding of each other to Flavocytb_{558}). Moreover, the same model was also able to reproduce all the kinetic data from Cross et al. [63,64] obtained using very different experimental conditions. Thus, we have extensively challenged our model with diverse

experimental data [59–64] to obtain a reliable and predictive model of NOX2 assembly and activation.

Integrated computational modelling of ROS production and scavenging from different sources provides a plausible mechanistic and quantitative framework for understanding the kinetic/molecular mechanisms regulating ROS homeostasis within cells/tissues under different assay conditions. We have recently developed and parameterized several computational models in this manner characterizing the kinetic/molecular mechanisms for the production and scavenging of ROS in the mitochondria [78–81]. The current model complements our recent NOX2 model [71], which characterized the thermodynamics of electron transfer from NADPH to O_2 through different redox centers of NOX2 complex (i.e. FAD and Cytb_{558} of Flavocytb_{558}) upon its assembly and activation. This model captured the dependence of NOX2 activity upon pH and temperature variations, and the distinct inhibitory effects of different drugs (DPI and GSK) on NOX2 activity. As with the current model, it was based on diverse published data on NOX2 kinetics obtained from a diversity of experimental conditions [58,72–77]. That model, however, did not consider the kinetics and regulation of different cytosolic subunit concentration-dependent assembly and activation of NOX2 facilitating $O_2^{\cdot -}$ production, the focus of the current study.

The present NOX2 assembly and activation model is significant in several aspects. First, the model integrates the interactions of all the cytosolic subunits with the membrane subunits based on a unified/generalized random rapid equilibrium binding mechanism. In contrast, the existing experimental studies have evaluated the kinetics of NOX2 assembly and activation using only a few cytosolic subunits in a given experimental system. No unified hypothesis regarding NOX2 assembly and activation mechanism has yet been proposed. For example, Cross et al. [47] proposed a special binding mechanism for NOX2 assembly and activation. Their kinetic scheme considered first essential binding of the subunit p47^{phox} to Flavocytb_{558}, and then random ordered binding of the subunits p67^{phox} and Rac to the complex. However, this scheme was unable to simulate the experimentally-measured changes in NOX2 activity ($O_2^{\cdot -}$ production) when the cytosolic subunits concentrations were varied [59–64]. It was for this reason that we considered an alternative kinetic mechanism, namely the generalized random rapid equilibrium binding mechanism, for the cytosolic subunits to bind to the membrane subunits toward NOX2 assembly and activation (Figure 2). This enabled development of an integrated model of NOX2 assembly and activation which was able to simulate changes in the experimentally-measured NOX2 activity and $O_2^{\cdot -}$ production with respect to varying cytosolic subunits concentrations in diverse experimental systems [59–64].

Other examples demonstrate the validity of the generalized random rapid equilibrium binding mechanism of the current model. Specifically, the subunit p40^{phox} was shown to be essential for NOX2 assembly and activation on the phagosomal membrane, but significantly less on the plasma membrane [55–57]. It was also found in cell-free systems that p40^{phox} enhances NOX2 activity by primarily enhancing the binding affinity of p47^{phox} for Flavocytb_{558} [64]. Remarkably, we were able to mathematically describe how p40^{phox} enhances the binding affinity of p47^{phox} for Flavocytb_{558} (Equation (3a)), which in turn

enhances NOX2 activity. Although we did not consider p40^{phox} was essential for NOX2 assembly and activation, the model can be easily extended as required to account for the p40^{phox} requirements for NOX2 assembly and activation on the phagosomal membranes [55–57]. Importantly, the present model appears to explain how and why NOX2 assembly and activation differs in different assay systems as a consequence of differences in the magnitudes of the kinetic parameters (e.g. apparent binding constants; Tables 1 and 2). The differences in the estimated apparent binding constants may be attributed to different affinities of the enzyme (Flavocytb_{558}) for the substrates (cytosolic subunits) as a consequence of varying molecular interactive forces between the enzyme and the substrates in these different assay systems.

A second important feature of the model is the regulatory control of NOX2 assembly and activation that accounts for the stimulatory and inhibitory interactions of guanine nucleotides (GTP and GDP) on the oxidase activation and subsequent $O_2^{\cdot -}$ production. Based on the kinetic data of Uhlinger et al. [60] and Peveri et al. [59], the model sheds light on the opposing effects of GTP and GDP on NOX2 activity and $O_2^{\cdot -}$ production. The model predictions suggest that 10 μM GTP is indeed required to maximally activate NOX2, while several orders of magnitude more GDP (>10 mM) is required to maximally inhibit NOX2. Moreover, there was an appreciable baseline NOX2 activity without any added GTP and GDP, due to the presence of ~0.5 μM baseline GTP (Figure 4). Furthermore, according to our model formulation, GTP not only enhances the binding of Rac to Flavocytb_{558}, but also enhances the bindings of p47^{phox} and p67^{phox} to Flavocytb_{558}, effectively enhancing the assembly and activation of NOX2 (Equation (3a–3c)). It is evident from the analysis that these events significantly affect the apparent kinetic parameters for these different cytosolic subunits binding to membrane Flavocytb_{558} (Figures 6–8).

Finally, the model accounted for a generalized mutual binding enhancement mechanism based on the studies of Uhlinger et al. [61] and Nisimoto et al. [62]. That is, the model simulated the influence of the subunits p47^{phox}, p67^{phox} and Rac upon each other's binding to the membrane subunits gp91^{phox} and p22^{phox} (Flavocytb_{558}) toward the oxidase activity (Figure 5 and Figures 6–8). Interestingly, the model predicted that the contribution of p47^{phox} toward p67^{phox} binding enhancement for Flavocytb_{558} is approximately 10-fold higher than the contribution of p67^{phox} towards p47^{phox} binding enhancement for Flavocytb_{558}. The model also predicted that there is no mutual binding enhancement between p47^{phox} and Rac, and only a negligible enhancement in the binding of Rac by p67^{phox}, but a significant enhancement in the binding of p67^{phox} by Rac (see Table 2). Overall, the model predicted that different cytosolic subunits differentially enhance the binding of the other cytosolic subunits to the membrane subunits in NOX2 assembly and activation characterized by different regulatory constants (see Table 2 and Appendix B).

Two sets of parameters are reported in Tables 1 and 2 corresponding to the two different types of datasets fitted to the model under different experimental conditions and protocols (i.e. Cross et al. [63,64] studies in fully recombinant cell-free systems vs. Uhlinger et al. [60,61], Peveri et al. [59], and Nisimoto et al. [62] studies in semi-recombinant cell-free systems that included isolated plasma membrane). Cross et al. datasets were not suitable to

characterize the regulatory mechanisms by guanine nucleotides (GTP and GDP) and mutual binding enhancements between the cytosolic subunits. This is because they varied only one subunit concentration while keeping all the other subunits and GTP at saturated concentrations in the absence of GDP. Thus, Equation (2) was only used to fit the datasets of Cross et al. In contrast, Equation (2) along with regulatory mechanisms incorporated into Equation (3a–3c) were used to jointly fit the datasets of Uhlinger et al. [60,61], Peveri et al. [59], and Nisimoto et al. [62]. Based on our hybrid approach of Monte-Carlo–Fmincon simulations, we were able to obtain unique estimates of the model parameters characterizing each of these two distinct cell-free systems for NOX2 assembly and activation. For robust estimation of the model parameters, some parameters were assumed to be fixed, which are mentioned in the tables, determined from the experimental conditions/protocols (i.e. Flavocytb_{558} concentrations, baseline cytosolic subunits concentrations, baseline GTP and GDP concentrations, and Hill's coefficients for regulation by GTP and GDP), and the rest of the parameters were left adjustable.

The logic behind fixing the baseline concentrations of Rac (for the experimental data of Uhlinger et al. [60]) and p47^{phox} (for the experimental data of Nisimoto et al. [62]) at negligible levels is that, based on our model (Equation (2)), Rac and p47^{phox} are essential for the assembly and activation of NOX2, yet these subunits were not added to the experimental protocols and assumed only to be present at negligible concentrations. Similarly, for some experiments of Uhlinger et al. [60], no GTP was added to the experimental protocol, yet significant baseline NOX2 activity was reported due to the presence of appreciable concentration of endogenous GTP, giving rise to about 50% of maximal NOX2 activity in the presence of high/saturable concentrations of GTP (10 μM). Thus, the baseline GTP concentration was fixed near the estimated K_{GTP} value for NOX2 assembly and activation. The logic behind fixing the Hill's coefficients for the enhancement of NOX2 assembly and activation by GTP at 2.0 and for the inhibition by GDP at 0.5 is that these values predict the accurate activation and inhibition profiles of NOX2 by GTP and GDP, respectively, as reported in Figure 4(C,D) without unnecessarily adding these parameters as unknown parameters for the estimation process. This enabled us to reduce the number of unknown parameters for estimation by two and also to break the correlation of these parameters with the regulatory constants for GTP and GDP (K_{GTP} and K_{GDP}) for NOX2 activation and inhibition, respectively. Thus, the estimates of the Hill's coefficients are deduced from the experimental data on GTP and GDP-dependent regulation of NOX2 activity (Figure 4(C,D)). Adding these parameters to the estimation process also gives the similar estimates as fixed.

Limitations

We recognize that the actual molecular mechanism involving the assembly and activation of NOX2 complex (E.p47.p67.Rac) may be more sophisticated than what is represented in our model that utilized a generalized random rapid equilibrium binding mechanism involving 12 individual reactions and 3 apparent binding constants K'_{p47}, K'_{p67} and K'_{Rac} (Figure 2). We have mathematically lumped several important aspects of the regulation of NOX2 assembly and activation. Specifically, we have lumped the uncertainties of the quantitative details of the 12 reactions into the three apparent binding constants (K'_{p47}, K'_{p67} and K'_{Rac}) for the

cytosolic subunits for the membrane subunits and the apparent catalytic constant for NOX2 (k_{NOX2}). These three binding constants were further related to the concentrations of the cytosolic subunits and the concentrations of GTP and GDP (Equation (3a–3c)), which enabled predictive simulations of an array of kinetic data from six different publications from four independent groups [59–64]. Consistent with the process of model building, the future iterations of this model can incorporate more details of the protein–protein interaction reactions, phosphorylation and dephosphorylation, alternative NOX2 assembly and activation mechanisms, and the regulation of the assembly and activation process by the Rho/Rac GTPase regulation cycle, as appropriate quantitative kinetic data becomes available.

An alternative assumption with the same random rapid equilibrium binding mechanism might be that the 12 individual reactions are characterized by 12 apparent binding constants $K'_{p47.n}$, $K'_{p67.n}$ and $K'_{Rac.n}$, $n = 1 \ldots 4$, satisfying 6 kinetic constraints involving the 6 rectangular surfaces of Figure 2 (6 microscopic balance constraints). So, without further simplification, this assumption leads to an increase in the number of unknown parameters in the model. In addition, one of the possible outcomes of this alternative assumption is that all the four apparent binding constants for each subunit may be equal. To illustrate this, consider the formation of the intermediate complex E.p47.p67 through the two different reaction sequences described above with the apparent binding constants $K'_{p47.1}$, $K'_{p47.2}$, $K'_{p67.1}$, and $K'_{p67.2}$. To satisfy the microscopic balance constraint, we must have $K'_{p47.1} \times K'_{p67.2} = K'_{p67.1} \times K'_{p47.2}$ (since both reaction sequences result in the same intermediate complex E.p47.p67). But this kinetic constraint indicates that both p47*phox* and p67*phox* would enhance the binding of each other to the same extent, which is not the case as illustrated through the results presented in Figures 6–7. Another possible outcome is that $K'_{p47.1} = K'_{p47.2}$ and $K'_{p67.1} = K'_{p67.2}$. The same analogy can be applied to the other intermediate complexes and the final NOX2 enzyme complex E.p47.p67.Rac to arrive at the same conclusion that all of the four apparent binding constants for each subunit may be equal. This assumption satisfies the microscopic and the overall balance constraints. The apparent binding constants are further functions of GTP, GDP, p47, p67, and Rac concentrations for the model to be able to describe all of the diverse experimental data simultaneously (Equation (3a–3c)). Therefore, we believe the ability of the developed model with hypothesized kinetic/regulation mechanisms to describe six different datasets [59–64] produced by four different groups is sufficient to ascertains the accuracy and the reliability of the model and kinetic/regulation mechanisms in describing the biological process of $O_2^{\cdot -}$ production on the cell membrane through the assembled and activated NOX2 complex.

Another limitation in our model is that the binding of the cytosolic subunits to the membrane subunits in forming the stable NOX2 complex in catalysing $O_2^{\cdot -}$ production may not all be rapidly equilibrating or even randomly ordered. The NOX2 assembly reactions *in vivo* may all be rate limiting. However, we analyzed kinetic data from several publications [59–64], and we were able to reproduce all the data with our model applying the generalized random rapid equilibrium binding assumption for NOX2 assembly and activation. This suggests that these data may not have sufficient information to evaluate the validity of such an assumption for computational modelling. We think that *in vivo* the slow or rate limiting nature of the

assembly reactions in cells may lead to reduced concentrations of the stable NOX2 complex in catalyzing $O_2^{\cdot -}$ production, which can be effectively accounted for by suitably reducing the catalytic constant (k_{NOX2}) for the $O_2^{\cdot -}$ production reaction or by suitably reducing the availability of the membrane subunit (E_0), without affecting the apparent binding constants (K's) for NOX2 assembly reactions. Another possibility would be to consider all the reactions involving NOX2 assembly (Figure 2) as rate limiting. But then this would lead to myriad of unknown parameters (twice the number of rate constants than binding constants) that would need to be estimated from the available data resulting in a model that would not be minimal or parsimonious and would have little predictive value. The publications [59–64] used in this modeling work as sources for the kinetic data, although in themselves are robust and rigorous, were conducted at a time when the components and assembly of NOX2 were less well understood, and consequently some of the components and their variations used in those studies may not completely fit with modern experimental approaches. On the other hand, the dearth of recent experimental studies providing amenable kinetic data means these are the best sources of data for further development of the model. This will enable more practical model based on current understanding of NOX2 assembly and activation.

Summary

A detailed mechanistic computational model was developed that incorporates diverse kinetic and regulatory mechanisms required for the assembly and activation of NOX2 facilitating $O_2^{\cdot -}$ production. The model accounts for the mutual interdependencies of NOX2 cytosolic subunits on NOX2 assembly and activation as well as regulations by guanine nucleotides. The model is capable of explaining kinetic data from diverse experimental systems with model simulations indicating that: (*i*) cytosolic subunits follow a random rapid equilibrium binding mechanism with their membrane counterparts towards NOX2 assembly and activation; (*ii*) guanine nucleotides are important regulators of NOX2 assembly and activation; (*iii*) cytosolic subunits $p47^{phox}$, $p67^{phox}$ and Rac differentially enhance the binding of one another's, with $p47^{phox}$ enhancing the binding affinity of $p67^{phox}$ an order of magnitude higher than $p47^{phox}$ enhancing the binding affinity of $p67^{phox}$ to the membrane subunits; (*iv*) Rac differentially enhances the binding affinity of $p47^{phox}$ and $p67^{phox}$ to the membrane subunits; (*v*) there is no mutual binding enhancement between $p47^{phox}$ and Rac; and (*vi*) $p40^{phox}$ enhances the binding affinity of $p47^{phox}$ to the membrane subunits, further enhancing NOX2 assembly and activation. The model therefore provides a mechanistic and quantitative framework to investigate the differential roles of different NOX2 subunits on its assembly and activation on the cell membrane facilitating $O_2^{\cdot -}$ production regulating diverse cellular mechanisms in a variety of conditions. The model also serves as a quantitative structure to expand upon in ways that would incorporate such concepts as membrane NOX and mitochondrial ROS-ROS crosstalk and interactions as encountered in conditions of health and disease. Ultimately, there is also a need for better quantitative kinetic data based on current understanding of NOX2 assembly and activation in order to test and further advance this mode

Funding

This work was supported by the National Institute of Health (NIH) grants P01-GM066730, P01-HL116264, and U01-HL122199.

Appendix A

This Appendix provides the mathematical derivation for the cytosolic subunits (p47^{phox}, p67^{phox}, and Rac)-dependent NOX2 complex formation and reaction flux expression under the condition of high (saturating) concentrations of the substrates NADPH and O_2 governed by the biochemical reaction: $NADPH + 2O_2 \leftrightarrow_{NOX2} NADP^+ + 2O_2^{\cdot -} + H^+$. Electron transfer from the substrate NADPH to O_2 occurs upon NOX2 assembly and activation, as depicted in Figure 2, in which p40^{phox} is not considered essential for NOX2 assembly and activation.

In addition, the proposed mechanism for NOX2 assembly and activation is based on random rapid equilibrium binding of the cytosolic subunits p47^{phox}, p67^{phox}, and Rac to the membrane components gp91^{phox} and p22^{phox} (complexed as E = gp91^{phox}.p22^{phox}), as described by the following elementary reactions:

$$E + p47 \underset{K'_{p47}}{\longleftrightarrow} E\,.\,p47 \tag{A1a}$$

$$E + p67 \underset{K'_{p67}}{\longleftrightarrow} E\,.\,p67 \tag{A1b}$$

$$E + Rac \underset{K'_{Rac}}{\longleftrightarrow} E\,.\,Rac \tag{A1c}$$

$$E\,.\,p47 + p67 \underset{K'_{p67}}{\longleftrightarrow} E\,.\,p47.p67 \tag{A1d}$$

$$E\,.\,p67 + p47 \underset{K'_{p47}}{\longleftrightarrow} E\,.\,p47.p67 \tag{A1e}$$

$$E\,.\,p47 + Rac \underset{K'_{Rac}}{\longleftrightarrow} E\,.\,p47.Rac \tag{A1f}$$

$$E\,.\,Rac + p47 \underset{K'_{p47}}{\longleftrightarrow} E\,.\,p47.Rac \tag{A1g}$$

$$E\,.\,p67 + Rac \underset{K'_{Rac}}{\longleftrightarrow} E\,.\,p67.Rac \tag{A1h}$$

$$E\,.\,Rac + p67 \underset{K'_{p67}}{\longleftrightarrow} E\,.\,p67.Rac \tag{A1i}$$

$$E\,.\,p47.p67 + Rac \underset{K'_{Rac}}{\longleftrightarrow} E\,.\,p47.p67.Rac \tag{A1j}$$

$$E\,.\,p47.Rac + p67 \underset{K'_{p67}}{\longleftrightarrow} E\,.\,p47.p67.Rac \tag{A1k}$$

$$E\,.\,p67.Rac + p47 \underset{K'_{p47}}{\longleftrightarrow} E\,.\,p47.p67.Rac \tag{A1l}$$

where K' s are the apparent dissociation/binding constants. Based on rapid equilibrium binding assumption, we have the following equilibrium relationships:

$$[E\,.\,p47] = \frac{[E][p47]}{K'_{p47}} \tag{A2a}$$

$$[E\,.\,p67] = \frac{[E][p67]}{K'_{p67}} \tag{A2b}$$

$$[E\,.\,Rac] = \frac{[E][Rac]}{K'_{Rac}} \tag{A2c}$$

$$[E\,.\,p47.p67] = \frac{[E][p47][p67]}{K'_{p47}K'_{p67}} \tag{A2d}$$

$$[E\,.\,p47.Rac] = \frac{[E][p47][Rac]}{K'_{p47}K'_{Rac}} \tag{A2e}$$

$$[E\,.\,p67.Rac] = \frac{[E][p67][Rac]}{K'_{p67}K'_{Rac}} \tag{A2f}$$

$$[E\,.\,p47.p67.Rac] = \frac{[E][p47][p67][Rac]}{K'_{p47}K'_{p67}K'_{Rac}} \tag{A2g}$$

The total NOX2 enzyme concentration is given by:

$$[E_{tot}] = [E] + [E\,.\,p47] + [E\,.\,p67] + [E\,.\,Rac] + [E\,.\,p47.p67] + [E\,.\,p47.Rac] + [E\,.\,p67.Rac] + [E\,.\,p47.p67.Rac] \tag{A3}$$

By substituting the expressions for the concentrations of different enzyme complexes from Equation (A2(a–g)) into Equation (A3), we have:

$$[E_{tot}] = [E]\left(1 + \frac{[p47]}{K'_{p47}} + \frac{[p67]}{K'_{p67}} + \frac{[Rac]}{K'_{Rac}} + \frac{[p47][p67]}{K'_{p47}K'_{p67}} + \frac{[p47][Rac]}{K'_{p47}K'_{Rac}} + \frac{[p67][Rac]}{K'_{p67}K'_{Rac}} + \frac{[p47][p67][Rac]}{K'_{p47}K'_{p67}K'_{Rac}}\right) \quad \text{(A4)}$$

This gives the expression for the free NOX2 enzyme concentration in terms of the total NOX2 enzyme concentration and the concentrations of different cytosolic NOX2 subunits:

$$[E] = \frac{[E_{tot}]}{\left(1 + \frac{[p47]}{K'_{p47}} + \frac{[p67]}{K'_{p67}} + \frac{[Rac]}{K'_{Rac}} + \frac{[p47][p67]}{K'_{p47}K'_{p67}} + \frac{[p47][Rac]}{K'_{p47}K'_{Rac}} + \frac{[p67][Rac]}{K'_{p67}K'_{Rac}} + \frac{[p47][p67][Rac]}{K'_{p47}K'_{p67}K'_{Rac}}\right)} \quad \text{(A5)}$$

Now, by substituting $[E]$ from Equation (5A) into Equation (A2g), we can express the concentration of the total assembled and activated NOX2 complex as:

$$[E\,.\,p47.p67.Rac] = \frac{[E_{tot}]\frac{[p47][p67][Rac]}{K'_{p47}K'_{p67}K'_{Rac}}}{\left(1 + \frac{[p47]}{K'_{p47}} + \frac{[p67]}{K'_{p67}} + \frac{[Rac]}{K'_{Rac}} + \frac{[p47][p67]}{K'_{p47}K'_{p67}} + \frac{[p47][Rac]}{K'_{p47}K'_{Rac}} + \frac{[p67][Rac]}{K'_{p67}K'_{Rac}} + \frac{[p47][p67][Rac]}{K'_{p47}K'_{p67}K'_{Rac}}\right)} \quad \text{(A6)}$$

Now, by multiplying the numerator and denominator of Equation (A6) by $K'_{p47}\,K'_{p67}K'_{Rac}$ and factoring out K'_{p47}, K'_{p67} and K'_{Rac} in separate steps, Equation (A6) can be simplified to:

$$[E\,.\,p47.p67.Rac] = [E_{tot}]\left(\frac{[p47]}{K'_{p47} + [p47]}\right)\left(\frac{[p67]}{K'_{p67} + [p67]}\right)\left(\frac{[Rac]}{K'_{Rac} + [Rac]}\right) \quad \text{(A7)}$$

At high (saturating) concentrations of the substrates NADPH and O_2, the overall NOX2 reaction flux is proportional to $[E.p47.p67.Rac]$, and hence can be expressed as:

$$J_{NOX2} = k_{NOX2}[E_{tot}]\left(\frac{[p47]}{K'_{p47} + [p47]}\right)\left(\frac{[p67]}{K'_{p67} + [p67]}\right)\left(\frac{[Rac]}{K'_{Rac} + [Rac]}\right) \quad \text{(A8)}$$

where k_{NOX2} is NOX2 catalytic constant at high NADPH and O_2 concentrations. At limiting or sub-saturating concentrations of the substrates NADPH and O_2, NOX2 catalytic constant k_{NOX2} would be a function of [NADPH] and [O_2], as developed in our recent publication [71].

Appendix B

This Appendix provides information on how the regulatory effects of guanine nucleotides (GTP, GDP) and cytosolic subunits (p40^{phox}, p47^{phox}, p67^{phox}, and Rac) on NOX2 reaction

flux were implemented in Equation (A8) to develop the final model presented in Equations (2), (3a), (3b), and (3c). This required the following steps: first, only the regulatory effects of guanine nucleotides were included resulting in Model 1; second, the regulatory effects of the same extent mutual binding enhancements between cytosolic subunits were implemented in Model 1 resulting in Model 2; third, the regulatory effects of the different extent mutual binding enhancements between cytosolic subunits were implemented in Model 1 resulting in Model 3. Each subsequent model, which is a nested version of the previous model, has more unknown parameters compared to the previous model, resulting in a better fit of the model to the experimental datasets. We also performed statistical tests, such as the *F*-test and the Akaike's information criterion (AIC) to compare the performance of Model 3 with its nested version (Model 2) and prove its superior fittings to the pertinent datasets. A hybrid approach of Monte-Carlo simulations and "fmincon" optimizer in MATLAB for parameter estimation is used in addition to computing the correlation coefficient matrix (CCM) to obtain the degree of interdependence between the model parameters.

Model 1: Regulations of cytosolic subunits binding by guanine nucleotides, without any mutual binding enhancements.

In this model, the regulatory effects of guanine nucleotides (GTP, GDP) are accounted for. As mentioned in the main text, based on the experimental data of Uhlinger et al. [60], GTP enhances the binding of cytosolic subunits ($p47^{phox}$, $p67^{phox}$, and Rac) to the membrane subunits ($p22^{phox}$ and $gp91^{phox}$), while GDP inhibits the binding of these cytosolic subunits. These regulatory effects are implemented by phenomenologically expressing the apparent binding constants K'_{p47}, K'_{p67}, and K'_{Rac} based on the standard Michaelis-Menten kinetic formulation for activation by GTP and inhibition by GDP as following:

$$K'_{p47} = K_{p47} / \left(\frac{C_{GTP}^{nT}}{K_{GTP}^{nT} + C_{GTP}^{nT}} \right) \left(\frac{K_{GDP}^{nD}}{K_{GDP}^{nD} + C_{GDP}^{nD}} \right) \tag{B1}$$

$$K'_{p67} = K_{p67} / \left(\frac{C_{GTP}^{nT}}{K_{GTP}^{nT} + C_{GTP}^{nT}} \right) \left(\frac{K_{GDP}^{nD}}{K_{GDP}^{nD} + C_{GDP}^{nD}} \right) \tag{B2}$$

$$K'_{Rac} = K_{Rac} / \left(\frac{C_{GTP}^{nT}}{K_{GTP}^{nT} + C_{GTP}^{n}} \right) \left(\frac{K_{GDP}^{nD}}{K_{GDP}^{nD} + C_{GDP}^{nD}} \right) \tag{B3}$$

where C_{GTP} and C_{GDP} denote the concentrations of GTP and GDP, respectively; K_{GTP} and K_{GDP} denote the regulatory constants for GTP and GDP to enhance and inhibit NOX2 activity, respectively; nT and nD are the corresponding Hill coefficients. This model (Model 1), without any mutual binding enhancements, was used to fit jointly to the experimental datasets of Uhlinger et al. [60,61], Peveri et al. [59], and Nisimoto et al. [62] to estimate the unknown parameters of the model. However, it was not able to describe well these datasets without any mutual binding enhancements by cytosolic subunits, resulting in a large sum of

squared differences error of 7.54, obtained by the “fmincon” optimization algorithm in MATLAB 2018b.

Model 2: Same extent mutual binding enhancements between cytosolic subunits (each subunit enhancing the binding of other subunits to the same extent).

In order to improve the model fits and reduce the sum of squared differences error from the model fittings to the available experimental data described above, we accounted for the regulatory effects of cytosolic subunits (p47^{phox}, p67^{phox}, and Rac) on one another’s binding to the membrane subunits (p22^{phox} and gp91^{phox}). As described in the main texts, based on Uhlinger et al. [61] studies, binding of p47^{phox} enhances the binding of p67^{phox} to the membrane subunits and vice versa (mutual binding enhancement), which we hypothesized to exist between all three cytosolic subunits (p47^{phox}, p67^{phox}, and Rac) for the sake of generality. To account for this mutual binding enhancement mechanism in the model, we assumed that p47^{phox} binding enhances p67^{phox} binding to the membrane subunits to the same extent as p47^{phox} binding enhances Rac binding to the membrane subunits, referred here as the same extent mutual binding enhancement hypothesis, which is accounted for in the binding constants K'_{p47}, K'_{p67}, and K'_{Rac} as following:

$$K'_{p47} = K_{p47}/\left(\frac{C_{GTP}^{nT}}{K_{GTP}^{nT}+C_{GTP}^{nT}}\right)\left(\frac{K_{GDP}^{nD}}{K_{GDP}^{nD}+C_{GDP}^{nD}}\right)\left(\frac{C_{p67}}{K''_{p67}+C_{p67}}\right)\left(\frac{C_{Rac}}{K''_{Rac}+C_{Rac}}\right) \quad \text{(B4)}$$

$$K'_{p67} = K_{p67}/\left(\frac{C_{GTP}^{nT}}{K_{GTP}^{nT}+C_{GTP}^{nT}}\right)\left(\frac{K_{GDP}^{nD}}{K_{GDP}^{nD}+C_{GDP}^{nD}}\right)\left(\frac{C_{p47}}{K''_{p47}+C_{p47}}\right)\left(\frac{C_{Rac}}{K''_{Rac}+C_{Rac}}\right) \quad \text{(B5)}$$

$$K'_{Rac} = K_{Rac}/\left(\frac{C_{GTP}^{nT}}{K_{GTP}^{nT}+C_{GTP}^{nT}}\right)\left(\frac{K_{GDP}^{nD}}{K_{GDP}^{nD}+C_{GDP}^{nD}}\right)\left(\frac{C_{p67}}{K''_{p67}+C_{p67}}\right)\left(\frac{C_{p47}}{K''_{p47}+C_{p47}}\right) \quad \text{(B6)}$$

where K''_{p47}, K''_{p67} and K''_{Rac} are the regulatory constants for p47^{phox}, p67^{phox} and Rac, respectively, characterizing the regulations of each other’s binding to Flavocytb_{558}; C_{p47} and C_{p67} and C_{Rac} are the concentrations of p47^{phox}, p67^{phox} and Rac, respectively. This model (Model 2) was used to fit jointly to the experimental datasets by Uhlinger et al. [60,61], Peveri et al. [59], and Nisimoto et al. [62] to estimate the unknown parameters of the model. It was able to describe the datasets by Uhlinger et al. and Peveri et al. on the GTP and GDP regulatory effects and cytosolic subunits mutual binding enhancements, but not the datasets by Nisimoto et al. on the cytosolic subunits mutual binding enhancements with the sum of squared differences error of 5.85, obtained by the “fmincon” optimization algorithm in MATLAB 2018 b.

Table B1.

Statistical comparison between Model 2 and Model 3 through *F*-test, fitted jointly to the experimental data of Uhlinger et al. [60,61], Peveri et al. [59], and Nisimoto et al. [62].

Model	SSD	Number of parameters	Number of data points	DF	*F* ratio	*p* Value
2	5.85	9	176	167	51.58	<0.0001
3	3.01	12	176	164		

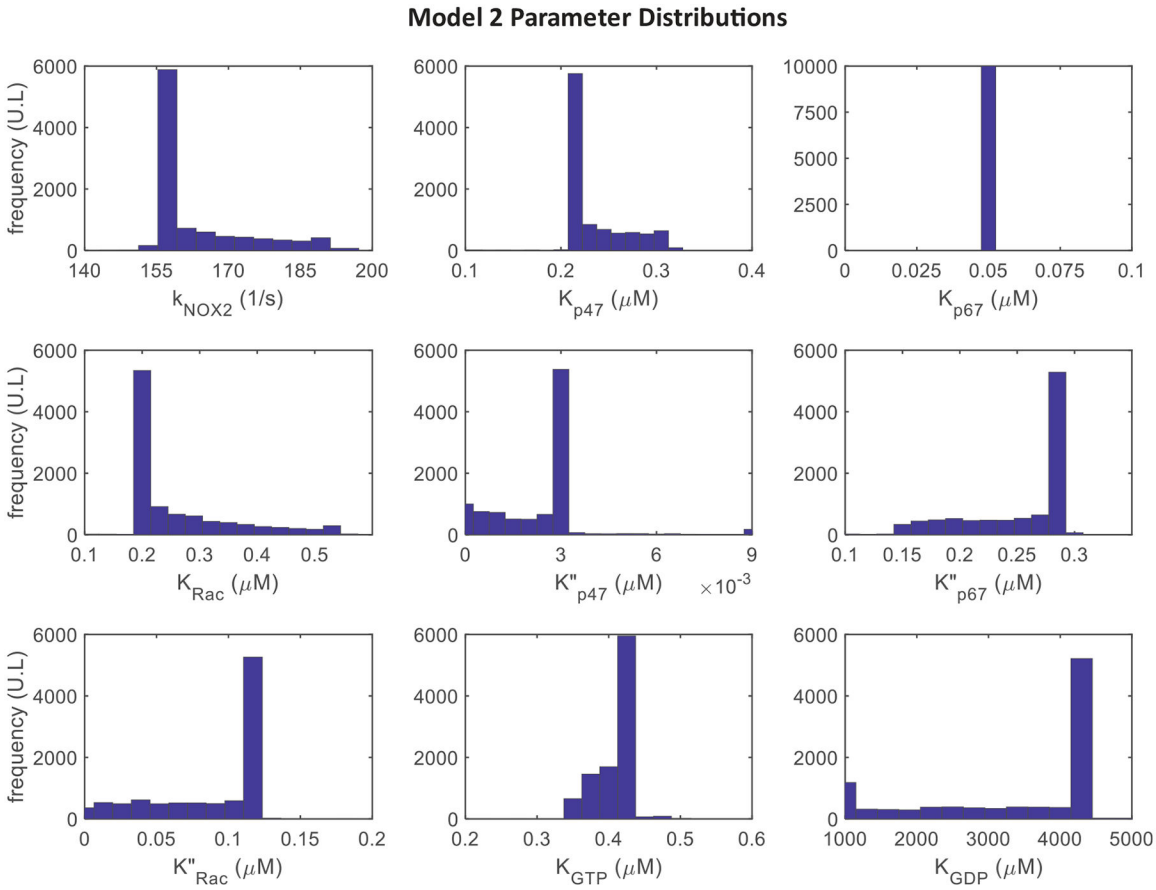

Figure B1.

Distribution of Model 2 estimated parameter values based on a hybrid Monte-Carlo-Fmincon simulations method. Plots show the distribution of the 9 estimated unknown parameter values for Model 2 fitted to experimental data of Uhlinger et al. [60, 61], Peveri et al. [59], and Nisimoto et al. [62] using a hybrid approach of Monte-Carlo simulations and "fmincon" optimization algorithm in MATLAB. The model is provided with 10,000 sets of 9 random initial values between 0 and 1 and the unknown parameters are estimated by "fmincon" optimizer for every set resulting in the values with the most probability of occurrence. For every parameter, the value with more than 55% probability of occurrence is indicated *via* the highest histogram bars that are also reported as the final estimated parameter values in Table 2. In this model, K_{p67} is fixed at 0.05 μ*M* and the rest of parameters are estimated.

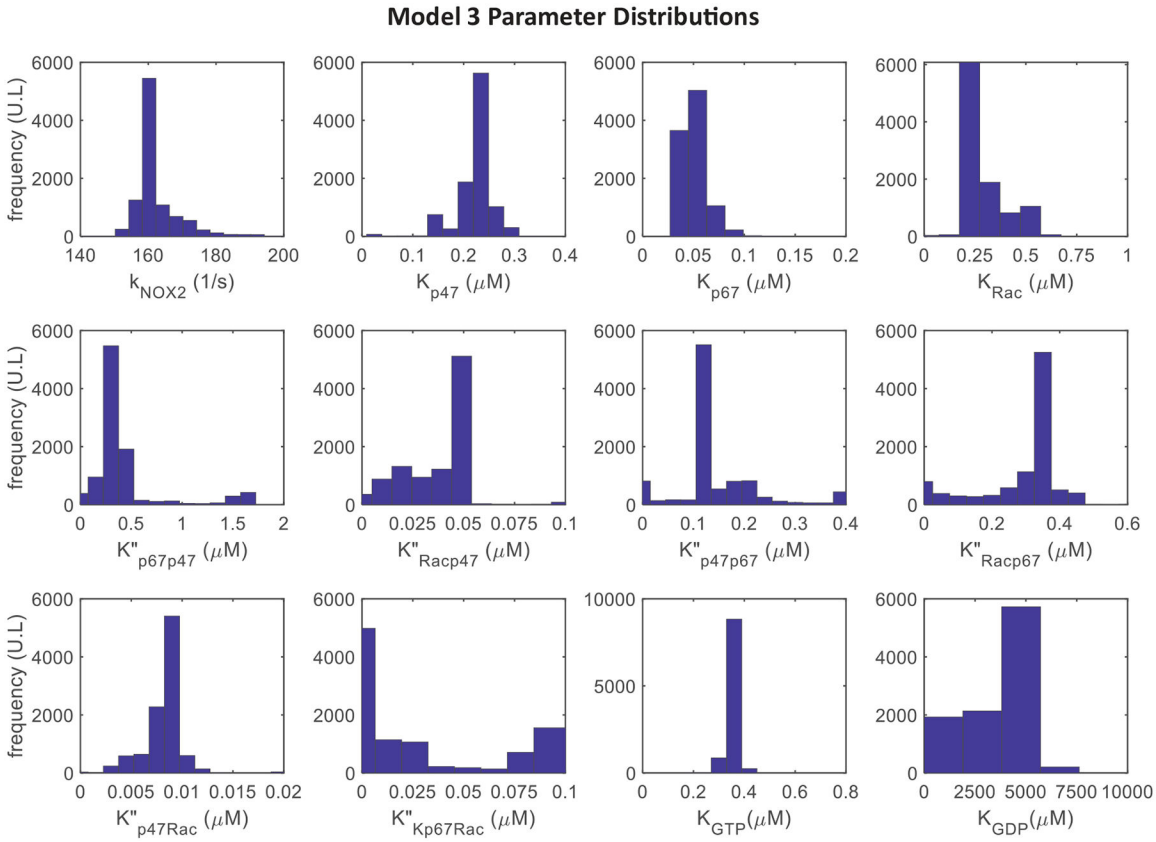

Figure B2.

Distribution of Model 3 estimated parameter values based on a hybrid Monte-Carlo–Fmincon simulations method. Plots show the distribution of the 12 estimated unknown parameter values for Model 3 fitted to the experimental data of Uhlinger et al. [60,61], Peveri et al. [59], and Nisimoto et al. [62] using a hybrid approach of Monte-Carlo simulations and “fmincon” optimization algorithm in MATLAB. The model is provided with 10,000 sets of 12 random initial values between 0 and 1 and the unknown parameters are estimated by “fmincon” optimizer for every set resulting in the values with the most probability of occurrence. For every parameter, the value with more than 55% probability of occurrence is indicated *via* the highest histogram bars that are also reported as the final estimated parameter values in Table 2.

Model 3: Different extent mutual binding enhancements between cytosolic subunits.

Based on the fits using Model 2, it was clear that the extent to which p47^{phox} enhances the binding of p67^{phox} is not the same as p67^{phox} enhancing the binding of p47^{phox} to the membrane subunits, which is true for all three cytosolic subunits. This difference provides the basis to further improve Model 2 by allowing for differential mutual binding enhancements between cytosolic subunits as following:

$$K'_{p47} = K_{p47} / \left(\frac{C_{GTP}^{nT}}{K_{GTP}^{nT} + C_{GTP}^{nT}} \right) \left(\frac{K_{GDP}^{nD}}{K_{GDP}^{nD} + C_{GDP}^{nD}} \right) \left(\frac{C_{p67}}{K''_{p67p47} + C_{p67}} \right) \left(\frac{C_{Rac}}{K''_{Racp47} + C_{Rac}} \right) \quad \text{(B7)}$$

$$K'_{p67} = K_{p67} / \left(\frac{C_{GTP}^{nT}}{K_{GTP}^{nT} + C_{GTP}^{nT}} \right) \left(\frac{K_{GDP}^{nD}}{K_{GDP}^{nD} + C_{GDP}^{nD}} \right) \left(\frac{C_{p47}}{K''_{p47p67} + C_{p47}} \right) \left(\frac{C_{Rac}}{K''_{Racp67} + C_{Rac}} \right) \quad \text{(B8)}$$

$$K'_{Rac} = K_{Rac} / \left(\frac{C_{GTP}^{nT}}{K_{GTP}^{nT} + C_{GTP}^{nT}} \right) \left(\frac{K_{GDP}^{nD}}{K_{GDP}^{nD} + C_{GDP}^{nD}} \right) \left(\frac{C_{p67}}{K''_{p67Rac} + C_{p67}} \right) \left(\frac{C_{p47}}{K''_{p47Rac} + C_{p47}} \right) \quad \text{(B9)}$$

where K''_{p67p47} and K''_{Racp47} are the regulatory constants for the p47^{phox} binding enhancements by p67^{phox} and Rac, respectively; K''_{p47p67} and K''_{Racp67} are the regulatory constants for the p67^{phox} binding enhancements by p47^{phox} and Rac, respectively; and K''_{p47Rac} and K''_{p67Rac} are the regulatory constants for the Rac binding enhancements by p47^{phox} and p67^{phox}, respectively. The resulting model (Model 3) was used to fit jointly to the experimental datasets by Uhlinger et al. [60,61], Peveri et al. [59], and Nisimoto et al. [62] to estimate the unknown parameters of the model. Model 3 was able to describe all the datasets on GTP and GDP regulatory effects as well as cytosolic subunits mutual binding enhancements with a very small sum of squared differences error of 3.01, obtained by the "fmincon" optimization algorithm in MATLAB 2018 b.

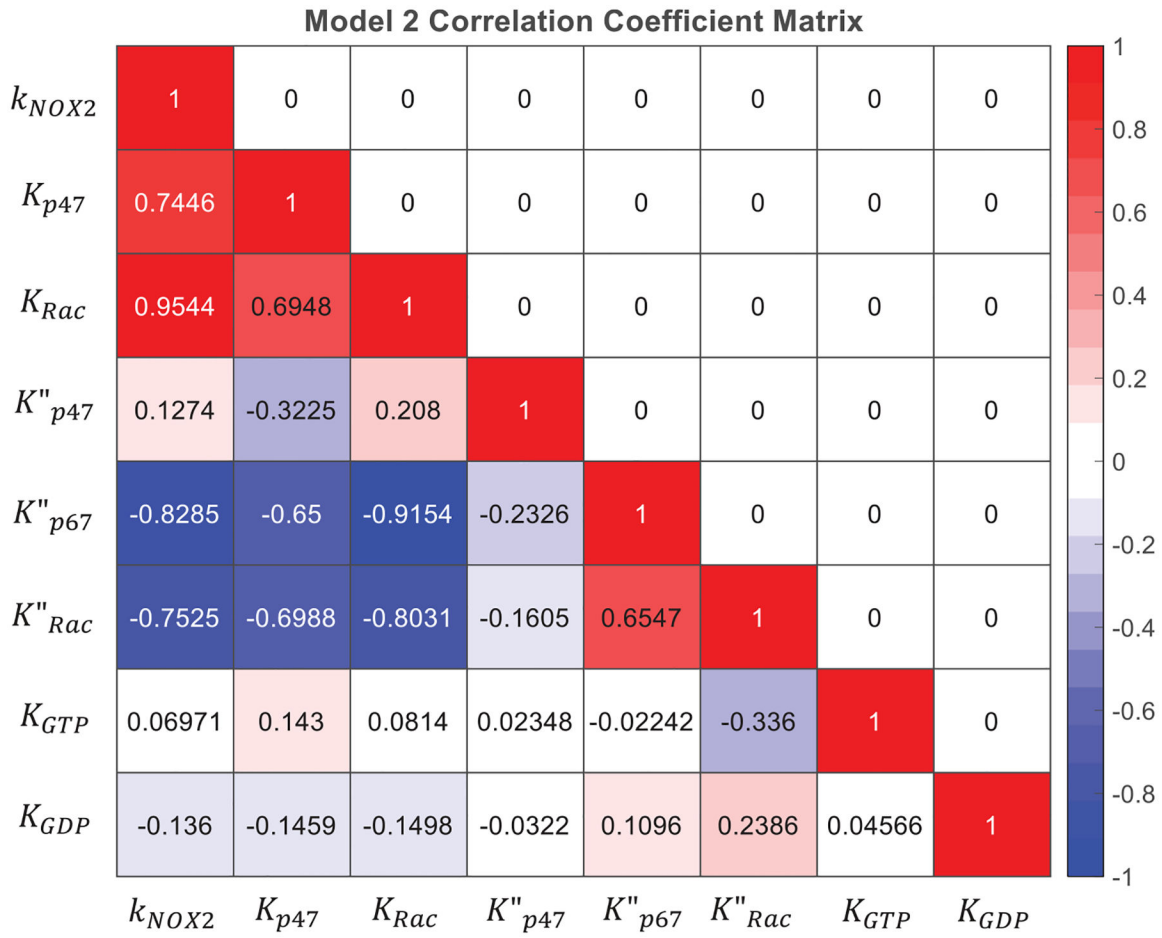

Figure B3.

Matrix of correlation coefficients between Model 2 parameters: The correlation coefficients between Model 2 parameters from Table 2 that best fit the model to the data is obtained using the “lsqcurvefit” algorithm. The correlation coefficients are in the range of −1 to +1 indicated with red color showing positive correlation in the range of 0 to +1; the blue color showing negative correlation in the range of 0 to −1; and the darker colors show higher correlation close to either ±1. The diagonal of the matrix shows the correlation of each parameter with itself which is 1. Also, since the matrix is symmetric, the upper triangle is put values equal to 0 for simplicity. Small correlation coefficients show small interdependence between the model parameters. In this model, K_{p67} is fixed and its correlation with other parameters cannot be calculated, and hence is removed.

Regulatory effect of p40^{phox} on p47^{phox} binding.

Based on the experimental datasets published by Cross et al. [64], p40^{phox} participates in activating NOX2 primarily by enhancing the binding affinity of p47^{phox} to the membrane subunits. This regulatory effect is accounted for *via* p47^{phox} binding affinity, as described in Equation (3a), to fit the model to the datasets by Cross et al. in which p40^{phox} is present. In order to fit the same model to Uhlinger et al. [60,61], Peveri et al. [59], and Nisimoto et al. [62] datasets in which p40^{phox} was not present, the last term in Equation (3a) is set to 1 (i.e.

$C_{p40} = 0$). Hence, the same model is able to describe and fit different datasets under different experimental conditions such as cell-free and reconstituted cell-based systems.

Comparison of the model fits for the three models.

Model 3 provided a better fit to the datasets (Figures 3, 4 and 5) than Model 2, resulting in a smaller sum of squared differences error. This is not surprising since Model 2 is a nested version of Model 3, and hence Model 3 has more unknown parameters. To determine whether the improvement in the fit using Model 3 as compared to the fit using Model 2 is large enough to justify the larger number of unknown parameters, we performed an *F*-test (Equation (B10)):

$$F = \frac{(SSD_2 - SSD_3)/(DF_3 - DF_2)}{SSD_2/DF_2} \tag{B10}$$

where *SSD2* and *SSD3* are the sum of squared differences between data and Model 2 fit and Model 3 fit, respectively; *DF2* and *DF3* are the degrees of freedom for Model 2 and Model 3, respectively [82]. *P* value is the probability of null hypothesis to be correct with significance level ($p = 0.05$; 95% confidence). Thus, the *F*-test takes into account the sum of squared differences, number of model parameters, and number of data points to compare two models and determine whether Model 3 is statistically a better model for the data in Figures 3, 4 and 5 than Model 2 [82]. Based on *F*-test for Model 2 and Model 3 in Table B1, the *P* value is less than 0.05 showing that the alternative hypotheses on Model 3 providing a significantly better fit than Model 2 is correct.

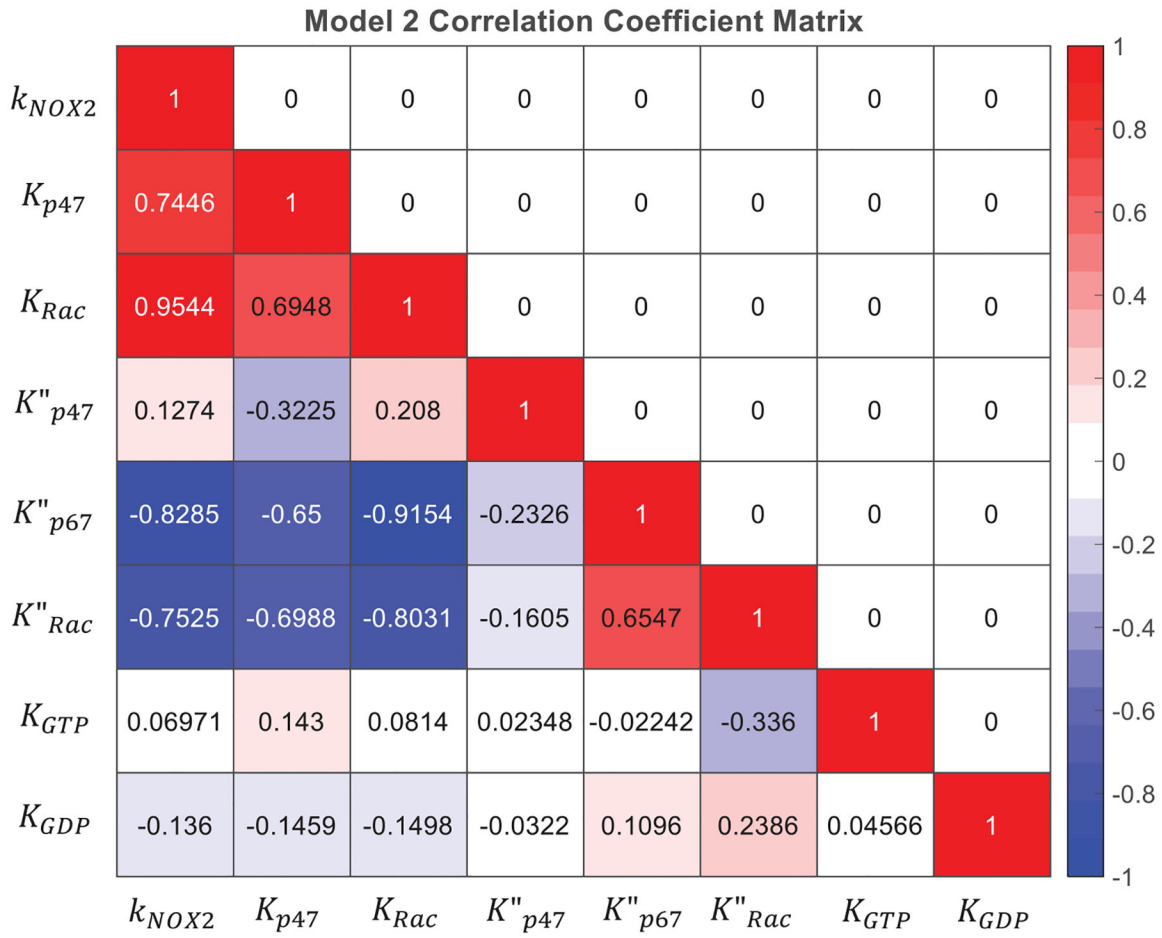

Figure B4.

Matrix of correlation coefficients between Model 3 parameters. The correlation coefficients between Model 3 parameters from Table 2 that best fit the model to the data is obtained using the “lsqcurvefit” algorithm. The correlation coefficients are in the range of −1 to +1 indicated with red color showing positive correlation in the range of 0 to +1; the blue color showing negative correlation in the range of 0 to −1; and the darker colors show higher correlation close to either ±1. The diagonal of the matrix shows the correlation of each parameter with itself which is 1. Also, since the matrix is symmetric, the upper triangle is put values equal to 0 for simplicity. Small correlation coefficients show small interdependence between the model parameters.

In the case of having two nested models, *F*-test is the proper test to compare the two models. However, AIC method is used for two or more number of nested and/or unrelated models. We also performed AIC test to compare the two models statistically based on Equation (B11):

$$AIC = N\ln\left(\frac{SSD}{N}\right) + 2K + \frac{2K(K+1)}{N-K-1} \tag{B11}$$

where N is the number of data points, K is the number of parameters, and SSD is the sum of squared differences for each model. The model with lower AIC is more likely to be correct. Based on the AIC values in Table 2, Model 3 is superior to Model 2. Therefore, based on both F-test and AIC results, Model 3 provides a significantly better fit to the pertinent data than Model 2. The fit of Model 1 to the data was visually bad enough that we did not attempt to compare it to that using Model 3.

Parameter estimation via hybrid Monte-Carlo–Fmincon simulations.

In order to estimate the unknown parameters of the three models, we used a hybrid approach of Monte-Carlo simulations and "fmincon" optimization algorithm. In doing this, we provided the model with 10,000 sets of random initial values uniformly distributed between 0 and 1 with the mean of 0.5 and standard deviation of 0.28. Using one set of random initial values, provided by the built-in "rand" function in MATLAB, the unknown parameters are estimated *via* the "fmincon" optimizer by minimizing the sum of squared differences between model simulations and data points resulting in one set of estimated parameters. This procedure was repeated for 10,000 iterations and the global estimates of the unknown parameters were those with the highest probability of occurrence. Figure B1 shows the distribution of Model 2 estimated parameters using this approach in which K'_{p67} was fixed at 0.05 and the rest of the 8 parameters were estimated. Figure B2 shows the distribution of Model 3 estimated parameters using the aforementioned approach in which all 12 parameters were estimated. The final parameters with the global least of the sum of squared differences are indicated in the histogram bars with highest frequency showing the highest probability of occurrence.

Correlation coefficient matrix.

The correlation coefficients (CC_{ij}) between the model parameters that best fit the model to the data were obtained using Equation (B12):

$$CC_{ij} = \frac{HH_{ij}}{\sqrt{HH_{ii} \times HH_{jj}}} \text{for} i, j = 1, \ldots, N \tag{B12}$$

where N is the number of model parameters and HH is the inverse of the product of Jacobian matrix and its transpose. Figures B3 and B4 show the correlation coefficient matrices for Model 2 and Model 3, respectively, obtained from the estimated parameter values in Table 2. Based on Model 2 correlation coefficient matrix, k_{NOX2} has high correlation with K_{Rac} and K''_{p67}, and K_{Rac} has high correlation with K''_{p67} and K''_{Rac}. Also, based on Model 3 correlation coefficient matrix, k_{Nox2} has high correlation with K_{Rac}, K''_{Racp47} and K''_{Racp67}; K_{Rac} has high correlation with K''_{Racp47} and K''_{Racp67}; and K_{p67} has high correlation with K''_{Racp67}, all of which were expected based on the interdependency of these parameters in Equations (B7–B9). However, for both the models, the correlation coefficients between several parameters are relatively small, indicating their independency of each other and their identifiability and estimability.

References

[1]. Murphy MP. How mitochondria produce reactive oxygen species. Biochem J. 2009;417(1):1–13. [PubMed: 19061483]

[2]. Stowe DF, Camara AK. Mitochondrial reactive oxygen species production in excitable cells: modulators of mitochondrial and cell function [invited comprehensive review]. Antioxid Redox Signal. 2009; 11(6):1373–1414. [PubMed: 19187004]

[3]. Figueira TR, Barros MH, Camargo AA, et al. Mitochondria as a source of reactive oxygen and nitrogen species: from molecular mechanisms to human health. Antioxid Redox Signal. 2013;18(16): 2029–2074. [PubMed: 23244576]

[4]. Lacy F, Gough DA, Schmid-Schönbein GW. Role of xanthine oxidase in hydrogen peroxide production. Free Radic Biol Med. 1998;25(6):720–727. [PubMed: 9801073]

[5]. Berry CE, Hare JM. Xanthine oxidoreductase and cardiovascular disease: molecular mechanisms and pathophysiological implications. J Physiol. 2004;555(Pt 3):589–606. [PubMed: 14694147]

[6]. Kelley EE, Khoo NK, Hundley NJ, et al. Hydrogen peroxide is the major oxidant product of xanthine oxidase. Free Radic Biol Med. 2010;48(4):493–498. [PubMed: 19941951]

[7]. Bokoch GM, Knaus UG. NADPH oxidases: not just for leukocytes anymore!. Trends Biochem Sci. 2003;28(9): 502–508. [PubMed: 13678962]

[8]. Lambeth JD. NOX enzymes and the biology of reactive oxygen. Nat Rev Immunol. 2004;4(3):181–189. [PubMed: 15039755]

[9]. Brandes RP, Kreuzer J. Vascular NADPH oxidases: molecular mechanisms of activation. Cardiovasc Res. 2005;65(1):16–27. [PubMed: 15621030]

[10]. Bedard K, Krause KH. The NOX family of ROS-generating NADPH oxidases: physiology and pathophysiology. Physiol Rev. 2007;87(1):245–313. [PubMed: 17237347]

[11]. Brandes RP, Weissmann N, Schroder K. Nox family NADPH oxidases: molecular mechanisms of activation. Free Radic Biol Med. 2014;76:208–226. [PubMed: 25157786]

[12]. Lambeth JD, Neish AS. Nox enzymes and new thinking on reactive oxygen: a double-edged sword revisited. Annu Rev Pathol. 2014;9:119–145. [PubMed: 24050626]

[13]. Bhattacharyya A, Chattopadhyay R, Mitra S, et al. Oxidative stress: an essential factor in the pathogenesis of gastrointestinal mucosal diseases. Physiol Rev. 2014;94(2):329–354. [PubMed: 24692350]

[14]. Bokoch GM. Regulation of innate immunity by Rho GTPases. Trends Cell Biol. 2005;15(3):163–171. [PubMed: 15752980]

[15]. Kohchi C, Inagawa H, Nishizawa T, et al. ROS and innate immunity. Anticancer Res. 2009;29(3):817–821. [PubMed: 19414314]

[16]. Bae YS, Oh H, Rhee SG, et al. Regulation of reactive oxygen species generation in cell signaling. Mol Cells. 2011;32(6):491–509. [PubMed: 22207195]

[17]. Ray PD, Huang BW, Tsuji Y. Reactive oxygen species (ROS) homeostasis and redox regulation in cellular signaling. Cell Signal. 2012;24(5):981–990. [PubMed: 22286106]

[18]. Brown DI, Griendling KK. Regulation of signal transduction by reactive oxygen species in the cardiovascular system. Circ Res. 2015;116(3):531–549. [PubMed: 25634975]

[19]. Yarosz EL, Chang CH. The role of reactive oxygen species in regulating T cell-mediated immunity and disease. Immune Netw. 2018;18(1):e14. [PubMed: 29503744]

[20]. Brown DI, Griendling KK. Nox proteins in signal transduction. Free Radic Biol Med. 2009;47(9):1239–1253. [PubMed: 19628035]

[21]. Carvalho DP, Dupuy C. Role of the NADPH oxidases DUOX and NOX4 in thyroid oxidative stress. Eur Thyroid J. 2013;2(3):160–167. [PubMed: 24847449]

[22]. Singel KL, Segal BH. NOX2-dependent regulation of inflammation. Clin Sci (Lond)). 2016;130(7):479–490. [PubMed: 26888560]

[23]. Lassegue B, Griendling KK. NADPH oxidases: functions and pathologies in the vasculature. Arterioscler Thromb Vasc Biol. 2010;30(4):653–661. [PubMed: 19910640]

[24]. Al Ghouleh I, Khoo NK, Knaus UG, et al. Oxidases and peroxidases in cardiovascular and lung disease: new concepts in reactive oxygen species signaling. Free Radic Biol Med. 2011;51(7):1271–1288. [PubMed: 21722728]

[25]. Sedeek M, Nasrallah R, Touyz RM, et al. NADPH oxidases, reactive oxygen species, and the kidney: friend and foe. J Am Soc Nephrol. 2013;24(10):1512–1518. [PubMed: 23970124]

[26]. Meitzler JL, Antony S, Wu Y, et al. NADPH oxidases: a perspective on reactive oxygen species production in tumor biology. Antioxid Redox Signal. 2014;20(17): 2873–2889. [PubMed: 24156355]

[27]. Thallas-Bonke V, Jandeleit-Dahm KA, Cooper ME. Nox4 and progressive kidney disease. Curr Opin Nephrol Hypertens. 2015;24(1):74–80. [PubMed: 25402870]

[28]. Audi SH, Friedly N, Dash RK, et al. Detection of hydrogen peroxide production in the isolated rat lung using Amplex red. Free Radic Res. 2018;52(9):1052–1062. [PubMed: 30175632]

[29]. Takac I, Schroder K, Zhang L, et al. The E-loop is involved in hydrogen peroxide formation by the NADPH oxidase Nox4. J Biol Chem. 2011;286(15): 13304–13313. [PubMed: 21343298]

[30]. Segal AW. The function of the NADPH oxidase of phagocytes and its relationship to other NOXs in plants, invertebrates, and mammals. Int J Biochem Cell Biol. 2008;40(4):604–618. [PubMed: 18036868]

[31]. Paffenholz R, Bergstrom RA, Pasutto F, et al. Vestibular defects in head-tilt mice result from mutations in Nox3, encoding an NADPH oxidase. Genes Dev. 2004; 18(5):486–491. [PubMed: 15014044]

[32]. Holterman CE, Thibodeau JF, Kennedy CR. NADPH oxidase 5 and renal disease. Curr Opin Nephrol Hypertens. 2015;24(1):81–87. [PubMed: 25415612]

[33]. Zheleznova NN, Yang C, Cowley AW. Jr., Role of Nox4 and p67phox subunit of Nox2 in ROS production in response to increased tubular flow in the mTAL of Dahl salt-sensitive rats. Am J Physiol Renal Physiol. 2016;311(2):F450–F458. [PubMed: 27279484]

[34]. Cowley AW Jr.,Yang C, Zheleznova NN, et al. Evidence of the importance of Nox4 in production of hypertension in Dahl salt-sensitive rats. Hypertension. 2016; 67(2):440–450. [PubMed: 26644237]

[35]. Touyz RM, Anagnostopoulou A, Camargo LL, et al. Vascular biology of superoxide-generating NADPH oxidase 5-implications in hypertension and cardiovascular disease. Antioxid Redox Signal. 2019;30(7): 1027–1040. [PubMed: 30334629]

[36]. Martner A, Aydin E, Hellstrand K. NOX2 in autoimmunity, tumor growth and metastasis. J Pathol. 2019; 247(2):151–154. [PubMed: 30270440]

[37]. van der Weyden L, Speak AO, Swiatkowska A, et al. Pulmonary metastatic colonisation and granulomas in NOX2-deficient mice. J Pathol. 2018;246(3):300–310. [PubMed: 30062795]

[38]. El-Benna J, Dang PM-C, Gougerot-Pocidalo M-A, et al. Francoise Braut-Boucher, p47phox, the phagocyte NADPH oxidase/NOX2 organizer: structure, phosphorylation and implication in diseases. Exp Mol Med. 2009;41(4):217. [PubMed: 19372727]

[39]. Juan D Matute AAA, Wright NAM, Wrobel I, et al. A new genetic subgroup of chronic granulomatous disease with autosomal recessive mutations in p40 phox and selective defects in neutrophil NADPH oxidase activity. Blood. 2009;114(15):3309–3315. [PubMed: 19692703]

[40]. Bromberg Y, Pick E. Unsaturated fatty acids stimulate NADPH-dependent superoxide production by cell-free system derived from macrophages. Cell Immunol. 1984;88(1):213–221. [PubMed: 6090027]

[41]. Bromberg Y, Pick E. Activation of NADPH-dependent superoxide production in a cell-free system by sodium dodecyl sulfate. J Biol Chem. 1985;260(25): 13539–13545. [PubMed: 2997168]

[42]. Koshkin V, Pick E. Generation of superoxide by purified and relipidated cytochrome b559 in the absence of cytosolic activators. FEBS Lett. 1993;327(1):57–62. [PubMed: 8392946]

[43]. Koshkin V, Pick E. Superoxide production by cytochrome b559. Mechanism of cytosol-independent activation. FEBS Lett. 1994;338(3):285–289. [PubMed: 8307196]

[44]. Koshkin V, Lotan O, Pick E. Electron transfer in the superoxide-generating NADPH oxidase complex reconstituted in vitro. Biochim Biophys Acta. 1997; 1319(2–3):139–146. [PubMed: 9131041]

[45]. Freeman JL, Lambeth JD. NADPH oxidase activity is independent of p47phox in vitro. J Biol Chem. 1996; 271(37):22578–22582. [PubMed: 8798426]

[46]. Cross AR, Curnutte JT. The cytosolic activating factors p47phox and p67phox have distinct roles in the regulation of electron flow in NADPH oxidase. J Biol Chem. 1995;270(12):6543–6548. [PubMed: 7896790]

[47]. Cross AR, Erickson RW, Curnutte JT. Simultaneous presence of p47(phox) and Flavocytochrome b-245 are required for the activation of NADPH oxidase by anionic amphiphiles. Evidence for an intermediate state of oxidase activation. J Biol Chem. 1999;274(22): 15519–15525. [PubMed: 10336445]

[48]. Dang PM, Cross AR, Quinn MT, et al. Assembly of the neutrophil respiratory burst oxidase: a direct interaction between p67PHOX and cytochrome b558 II. Proc Natl Acad Sci USA. 2002;99(7):4262–4265. [PubMed: 11917128]

[49]. Lapouge K, Smith SJM, Groemping Y, et al. Architecture of the p40-p47-p67phox complex in the resting state of the NADPH oxidase. A central role for p67phox, The. J Biol Chem. 2002;277(12):10121–10128. [PubMed: 11796733]

[50]. Quinn MT, Evans T, Loetterle LR, et al. Translocation of Rac correlates with NADPH oxidase activation. Evidence for equimolar translocation of oxidase components. J Biol Chem. 1993;268(28):20983–20987. [PubMed: 8407934]

[51]. Heyworth PG, Bohl BP, Bokoch GM, et al. Rac translocates independently of the neutrophil NADPH oxidase components p47phox and p67phox. Evidence for its interaction with Flavocytochrome b558. J Biol Chem. 1994;269(49):30749–30752. [PubMed: 7982999]

[52]. Ago T, Kuribayashi F, Hiroaki H, et al. Phosphorylation of p47phox directs phox homology domain from SH3 domain toward phosphoinositides, leading to phagocyte NADPH oxidase activation. Proc Natl Acad Sci USA. 2003;100(8):4474–4479. [PubMed: 12672956]

[53]. Groemping Y, Lapouge K, Smerdon SJ, et al. Molecular basis of phosphorylation-induced activation of the NADPH oxidase. Cell. 2003;113(3):343–355. [PubMed: 12732142]

[54]. Nauseef WM. Assembly of the phagocyte NADPH oxidase. Histochem Cell Biol. 2004;122(4):277–291. [PubMed: 15293055]

[55]. Belambri SA, Rolas L, Raad H, et al. NADPH oxidase activation in neutrophils: Role of the phosphorylation of its subunits. Eur J Clin Invest. 2018;48 Suppl 2: e12951. [PubMed: 29757466]

[56]. Tamura M, Shiozaki I, Ono S, et al. p40phox as an alternative organizer to p47phox in Nox2 activation: a new mechanism involving an interaction with p22phox. FEBS Lett. 2007;581(23):4533–4538. [PubMed: 17803994]

[57]. Li XJ, Marchal CC, Stull ND, et al. p47phox Phox homology domain regulates plasma membrane but not phagosome neutrophil NADPH oxidase activation. J Biol Chem. 2010;285(45):35169–35179. [PubMed: 20817944]

[58]. Suzuki Y, Lehrer RI. NAD(P)H oxidase activity in human neutrophils stimulated by phorbol myristate acetate. J Clin Invest. 1980;66(6):1409–1418. [PubMed: 6255012]

[59]. Peveri P, Heyworth PG, Curnutte JT. Absolute requirement for GTP in activation of human neutrophil NADPH oxidase in a cell-free system: role of ATP in regenerating GTP. Proc Natl Acad Sci USA. 1992;89(6): 2494–2498. [PubMed: 1312725]

[60]. Uhlinger DJ, Tyagi SR, Inge KL, et al. The respiratory burst oxidase of human neutrophils. Guanine nucleotides and arachidonate regulate the assembly of a multicomponent complex in a semirecombinant cell-free system. J Biol Chem. 1993;268(12):8624–8631. [PubMed: 8386165]

[61]. Uhlinger DJ, Taylor KL, Lambeth JD. p67-phox enhances the binding of p47-phox to the human neutrophil respiratory burst oxidase complex. J Biol Chem. 1994; 269(35):22095–22098. [PubMed: 8071333]

[62]. Nisimoto Y, Freeman JL, Motalebi SA, et al. Rac binding to p67(phox). Structural basis for interactions of the Rac1 effector region and insert region with components of the respiratory burst oxidase. J Biol Chem. 1997;272(30):18834–18841. [PubMed: 9228059]

[63]. Cross AR, Erickson RW, Curnutte JT. The mechanism of activation of NADPH oxidase in the cell-free system: the activation process is primarily catalytic and not through the formation of a stoichiometric complex, Biochem J. 1999;341(2):251–255. [PubMed: 10393079]

[64]. Cross AR. p40(phox) Participates in the activation of NADPH oxidase by increasing the affinity of p47(phox) for Flavocytochrome b(558). Biochem J. 2000;349(Pt 1): 113–117. [PubMed: 10861218]

[65]. Bokoch GM, Bohl BP, Chuang TH. Guanine nucleotide exchange regulates membrane translocation of Rac/Rho GTP-binding proteins. J Biol Chem. 1994;269(50): 31674–31679. [PubMed: 7989340]

[66]. Bokoch GM. Regulation of the human neutrophil NADPH oxidase by the Rac GTP-binding proteins. Curr Opin Cell Biol. 1994;6(2):212–218. [PubMed: 8024812]

[67]. Bokoch GM, Knaus UG. The role of small GTP-binding proteins in leukocyte function. Curr Opin Immunol. 1994;6(1):98–105. [PubMed: 8172686]

[68]. Gorzalczany Y, Sigal N, Itan M, et al. Targeting of Rac1 to the Phagocyte Membrane Is Sufficient for the Induction of NADPH Oxidase Assembly. J Biol Chem. 2000;275(51):40073–40081. [PubMed: 11007780]

[69]. Ugolev Y, Berdichevsky Y, Weinbaum C, et al. Dissociation of Rac1(GDP).RhoGDI complexes by the cooperative action of anionic liposomes containing phosphatidylinositol 3,4,5-trisphosphate, Rac guanine nucleotide exchange factor, and GTP. J Biol Chem. 2008;283(32):22257–22271. [PubMed: 18505730]

[70]. Pick E Role of the Rho GTPase Rac in the activation of the phagocyte NADPH oxidase: outsourcing a key task. Small GTPases. 2014;5:e27952. [PubMed: 24598074]

[71]. Tomar N, Sadri S, Cowley AW Jr, et al. A thermodynamically-constrained mathematical model for the kinetics and regulation of NADPH oxidase 2 complex-mediated electron transfer and superoxide production. Free Radic Biol Med. 2019;134:581–597. [PubMed: 30769160]

[72]. Babior BM, Curnutte JT, McMurrich BJ. The particulate superoxide-forming system from human neutrophils. Properties of the system and further evidence supporting its participation in the respiratory burst. J Clin Invest. 1976;58(4):989–996. [PubMed: 9426]

[73]. Bauldry SA, Nasrallah VN, Bass DA. Activation of NADPH oxidase in human neutrophils permeabilized with Staphylococcus aureus alpha-toxin. A lower Km when the enzyme is activated in situ. J Biol Chem. 1992;267(1):323–330. [PubMed: 1309741]

[74]. Morgan D, Cherny VV, Murphy R, et al. Temperature dependence of NADPH oxidase in human eosinophils. J Physiol. 2003;550(Pt 2):447–458. [PubMed: 12754316]

[75]. Morgan D, Cherny VV, Murphy R, et al. The pH dependence of NADPH oxidase in human eosinophils. J Physiol. 2005;569(Pt 2):419–431. [PubMed: 16195320]

[76]. Nisimoto Y, Diebold BA, Cosentino-Gomes D, et al. Nox4: a hydrogen peroxide-generating oxygen sensor. Biochemistry. 2014;53(31):5111–5120. [PubMed: 25062272]

[77]. Hirano K, Chen WS, Chueng AL, et al. Discovery of GSK2795039, a Novel Small Molecule NADPH Oxidase 2 Inhibitor. Antioxid Redox Signal. 2015;23(5):358–374. [PubMed: 26135714]

[78]. Bazil JN, Pannala VR, Dash RK, et al. Determining the origins of superoxide and hydrogen peroxide in the mammalian NADH:ubiquinone oxidoreductase. Free Radic Biol Med. 2014;77:121–129. [PubMed: 25236739]

[79]. Pannala VR, Bazil JN, Camara AK, et al. A biophysically based mathematical model for the catalytic mechanism of glutathione reductase. Free Radic Biol Med. 2013;65:1385–1397. [PubMed: 24120751]

[80]. Pannala VR, Bazil JN, Camara AK, et al. A mechanistic mathematical model for the catalytic action of glutathione peroxidase. Free Radic Res. 2014;48(4):487–502. [PubMed: 24456207]

[81]. Pannala VR, Dash RK. Mechanistic characterization of the thioredoxin system in the removal of hydrogen peroxide. Free Radic Biol Med. 2015;78:42–55. [PubMed: 25451645]

[82]. Harvey Motulsky AC. Fitting models to biological data using linear and nonlinear regression. New York (NY): Oxford University Press; 2004.

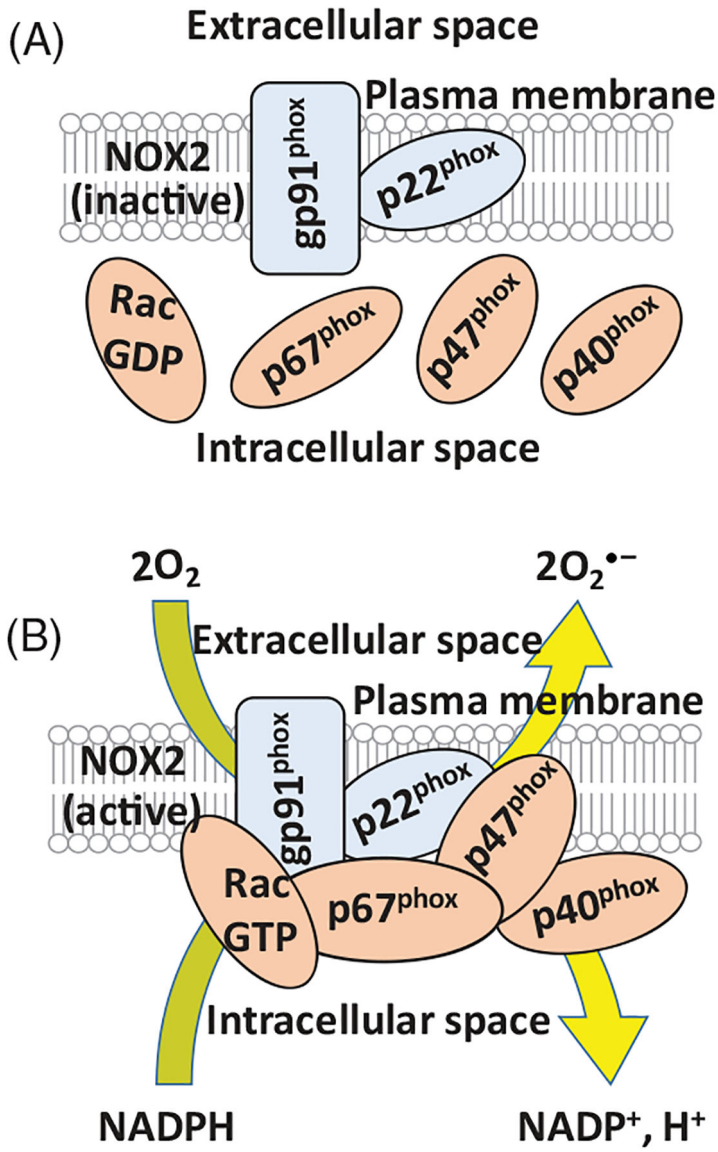

Figure 1.

NOX2 enzyme at resting and activated states. (A) Schematics shows NOX2 enzyme at resting state (unassembled and inactivated), where the membrane and cytosolic subunits are separated on the cell membrane and in the cytosol, respectively. Rac exists in an inactive GDP-bound form, and the p40*phox*, p47*phox* and p67*phox* subunits are also in inactive forms. (B) Schematics shows NOX2 enzyme complex upon assembly and activation, which facilitates electron transfer from the substrate NADPH to O_2 resulting in $O_2^{\cdot -}$ production. The activation of NOX2 requires the binding of activated p47*phox*, p67*phox* and Rac (GTP-bound form), and optionally activated p40*phox* that further enhances NOX2 activity, to the complex p22*phox*.p67*phox* on the cell membrane.

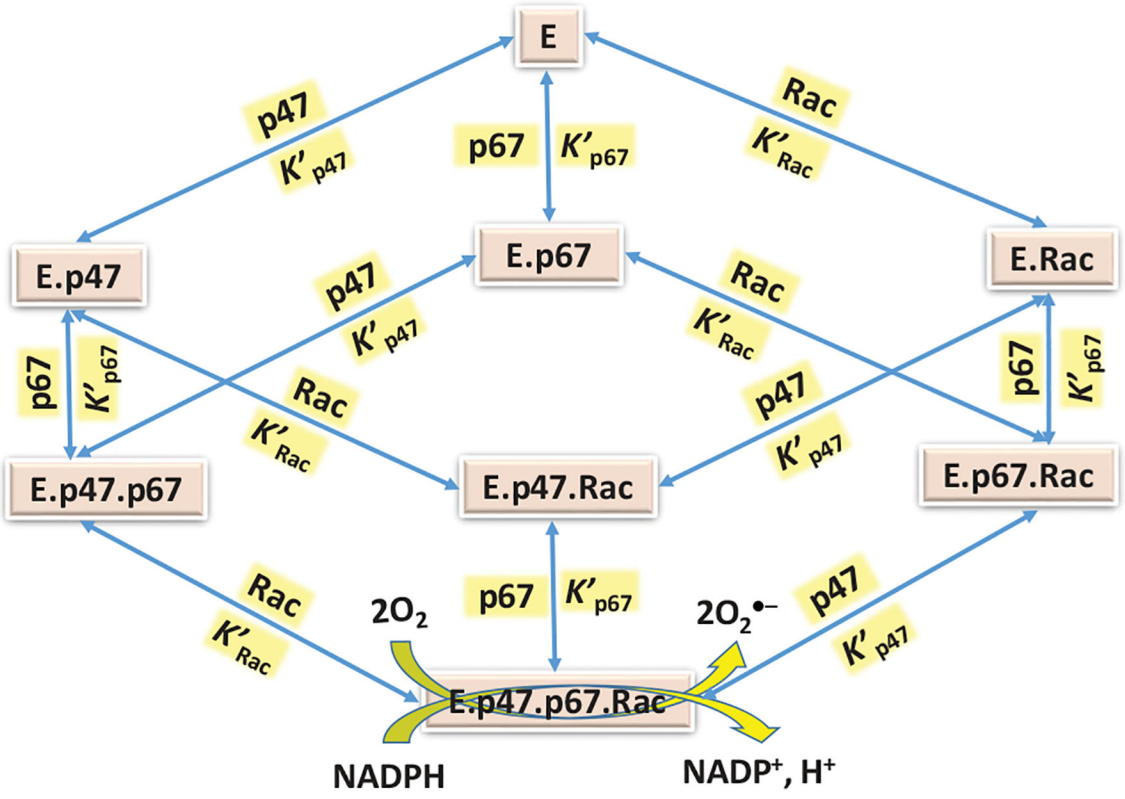

Figure 2.

Proposed kinetic mechanism for NOX2 assembly and activation facilitating superoxide production. Schematics shows our postulated generalized random rapid equilibrium binding mechanism for NOX2 assembly and activation, where E represents the membrane subunits complex p22^{phox}.gp91-^{phox}, which constitute flavocytochrome b_{558} (Flavocytb_{558}) to which the cytosolic subunits p47^{phox}, p67^{phox} and Rac bind upon their activation. As per the proposed mechanism, E can first bind to any of the NOX2 cytosolic subunits (p47^{phox}, p67^{phox}, Rac) in a rapid equilibrium manner and then the rest of the subunits can bind to the complex in a similar manner to form the highly activated multi-subunit enzyme complex E.p47^{phox}.p67^{phox}.Rac, with K'_i (i = p47^{phox}, p67^{phox}, Rac) representing the apparent dissociation constants for the respective subunits rapid equilibrium binding reactions with the membrane subunits. In the schematics, p47 = p47^{phox}, p67 = p67^{phox}, and Rac = Rac1 or Rac2.

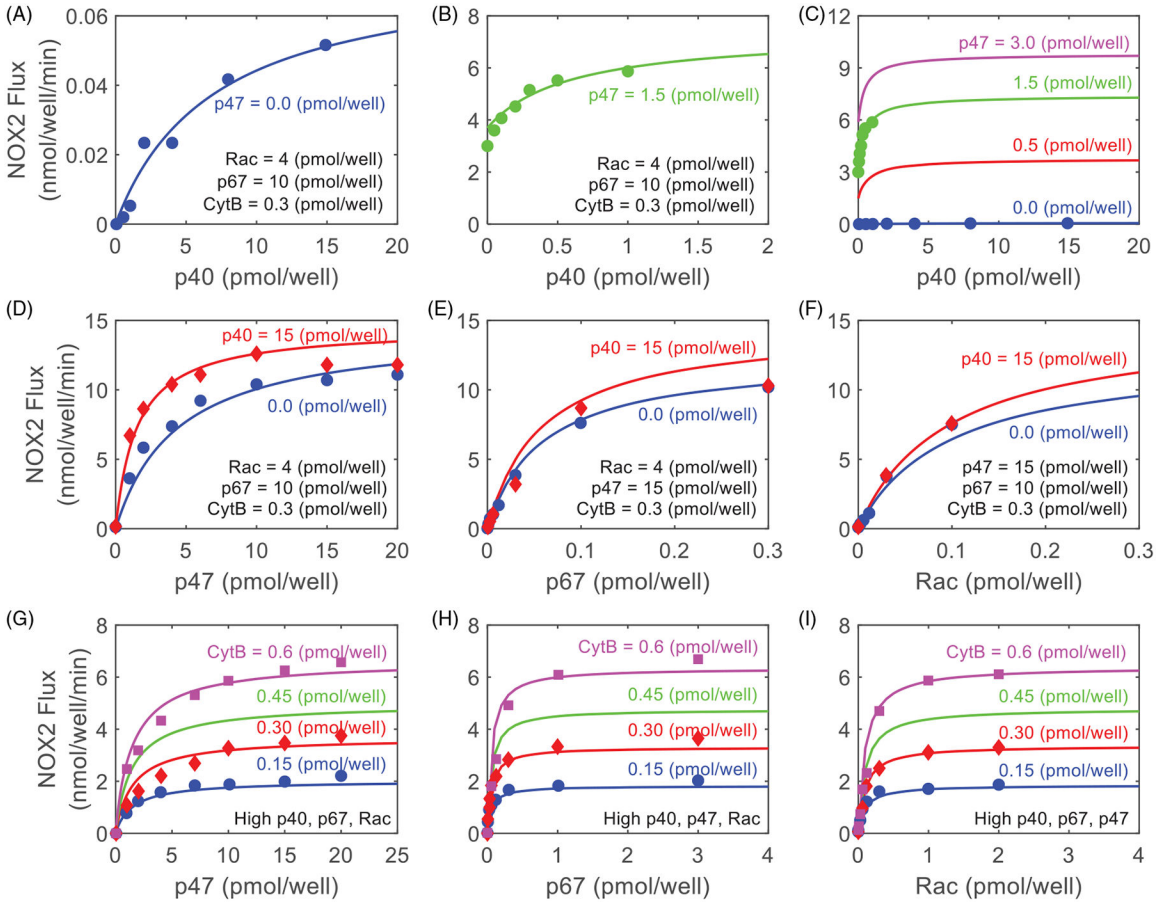

Figure 3.

Model fittings to the experimental data of Cross et al. [63,64] on the cytosolic subunit concentration-dependent NOX2 assembly, activation, superoxide production, and regulation by $p40^{phox}$ and $p47^{phox}$ interactions in cell-free systems. (A–C) Model simulations (lines) are compared to the experimental data (points) of Cross [64] on the effects of $p47^{phox}$ on the saturation kinetics and regulation of NOX2 reaction flux (rate of $O_2^{\cdot -}$ production) with respect to varying concentrations of $p40^{phox}$ at different concentrations of $p47^{phox}$ with fixed Rac concentration of 4 pmol/well, $p67^{phox}$ concentration of 10 pmol/well, and Flavocytb_{558} concentration of 0.3 pmol/well. Panels A and B are zoomed-in forms of Panel C for the concentration of $p47^{phox}$ at 0.0 pmol/well and 1.5 pmol/well, respectively. Where $p47^{phox}$ is zero, it is substituted with $p40^{phox}$ in Equation (2). (D–F) Model simulations (lines) are compared to the experimental data (points) of Cross [64] on the effects of $p40^{phox}$ on the saturation kinetics and regulation of NOX2 reaction flux (rate of $O_2^{\cdot -}$ production) with respect to varying concentrations of the subunits $p47^{phox}$, $p67^{phox}$ and Rac, respectively, at two different concentrations of $p40^{phox}$ (0 and 15 pmol/well) with fixed Flavocytb_{558} concentration of 0.3 pmol/well. In Panel D, concentrations of Rac and $p67^{phox}$ are fixed at 4 pmol/well and 10 pmol/well, respectively. In Panel E, concentrations of Rac and $p47^{phox}$ are fixed at 4 pmol/well and 15 pmol/well, respectively. In Panel F, concentrations of $p47^{phox}$ and $p67^{phox}$ are fixed at 15 pmol/well and 10 pmol/well, respectively. (G-I) Model simulations (lines) are compared to the experimental data (points) of Cross et al. [63] on the

effects of Flavocytb_{558} on the saturation kinetics and regulation of NOX2 reaction flux (rate of $O_2^{\cdot -}$ production) with respect to varying concentrations of the subunits p47^{phox}, p67^{phox} and Rac, respectively, at different concentrations of Flavocytb_{558}. In Panel G, p67^{phox}, p40^{phox} and Rac are present at high concentrations. In Panel H, p47^{phox}, p40^{phox} and Rac are present at high concentrations. In Panel I, p67^{phox}, p47^{phox} and p40^{phox} are present at high concentrations. Model-simulated lines for NOX2 flux for Flavocytb_{558} concentration of 0.6 pmol/well and 0.15 pmol/well are within ±10% of the reported values. Cross et al. [63,64] studied the kinetics and regulation of NOX2 assembly, activation, and $O_2^{\cdot -}$ production in a cell-free system, that is, in an *in vitro* 150 μL well containing different concentrations of Flavocytb_{558} and cytosolic subunits, as indicated in the plots. Model simulations were carried out using the estimated parameter values in Table 1.

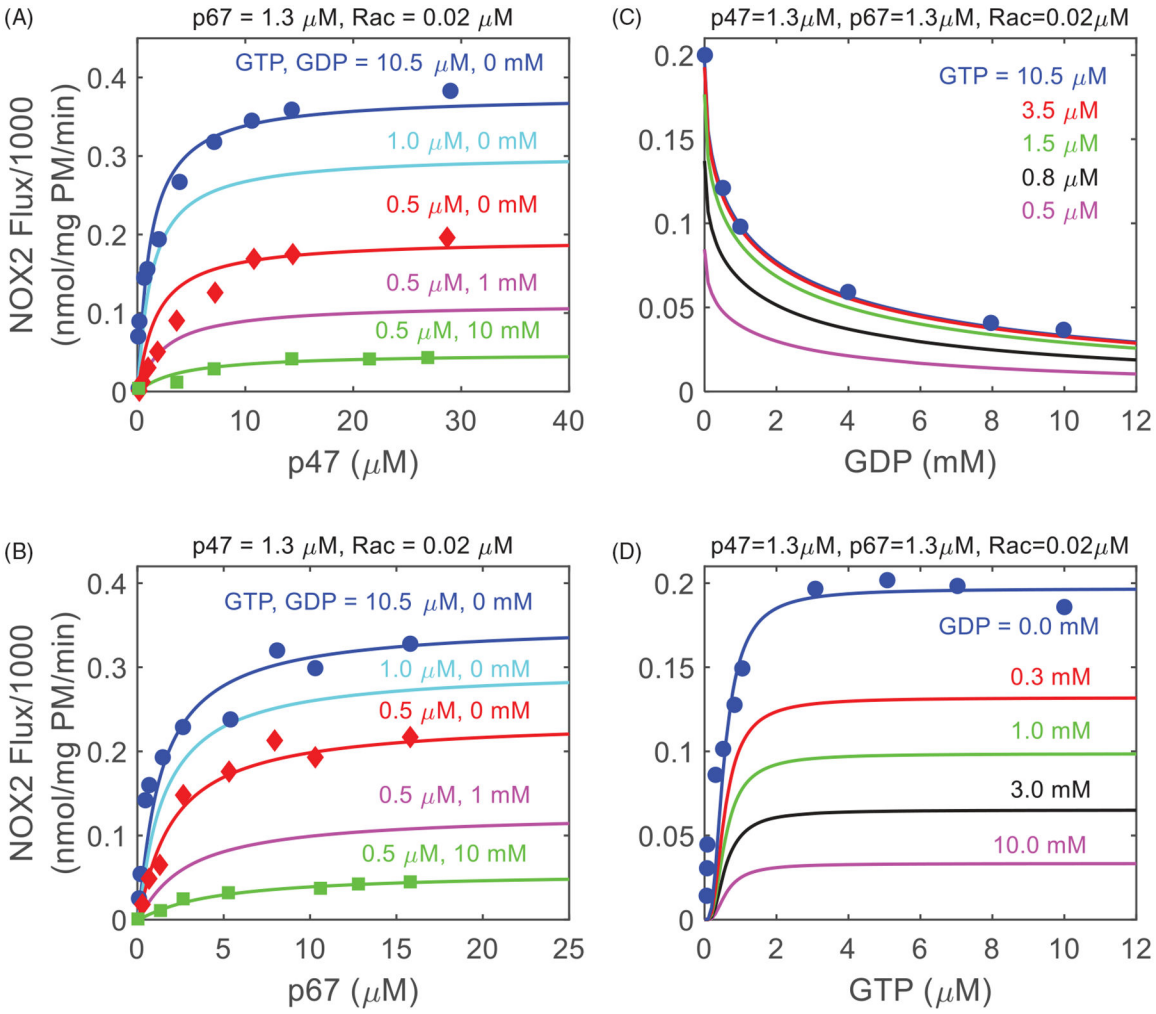

Figure 4.

Model fittings to the experimental data of Uhlinger et al. [60] and Peveri et al. [59] on the cytosolic subunit concentration-dependent NOX2 assembly, activation, ROS production, and their regulations by guanine nucleotides in cell-free systems. (A, B) Model simulations (lines) are compared to the experimental data (points) of Uhlinger et al. [60] on the regulatory effects of GTP and GDP on the saturation kinetics of NOX2 reaction flux (rate of $O_2^{\cdot -}$ production) with respect to varying concentration of the subunit $p47^{phox}$ with fixed $p67^{phox}$ concentration of 1.3 μM (A) and varying concentration of the subunit $p67^{phox}$ with fixed $p47^{phox}$ concentration of 1.3 μM (B), under the presence of a nominal Rac concentration of 0.02 μM. Varying concentrations of GTP and GDP or no nucleotide present were included, as indicated in the plots. Model-simulated lines for NOX2 flux are within ±10% of the reported values. (C, D) Model simulations demonstrating the roles of GDP as an inhibitory factor and GTP as a stimulatory factor for NOX2 assembly, activation, and $O_2^{\cdot -}$ production are compared to available experimental data [59,60], with the subunits $p47^{phox}$, $p67^{phox}$ and Rac concentrations are as indicated in the plots. In all experiments of Uhlinger et al. [60], 50 μl of reaction mixtures (pH = 7.4) contained 10 μg of plasma membrane (PM), or equivalently 8.6 pmol of Flavocytb_{558}, providing an appropriate

concentration of total NOX2 complex for model simulations. For the experimental data of Peveri et al. [59], NOX2 flux was multiplied by a factor of 5.7 to be in the same range of NOX2 flux as in the experimental data of Uhlinger et al. [60] for a comparative data analysis. In addition, the substrates NADPH and O_2 concentrations were very high (250 μM, saturated) in all experiments. Model simulations were carried out using the estimated parameter values in Table 2.

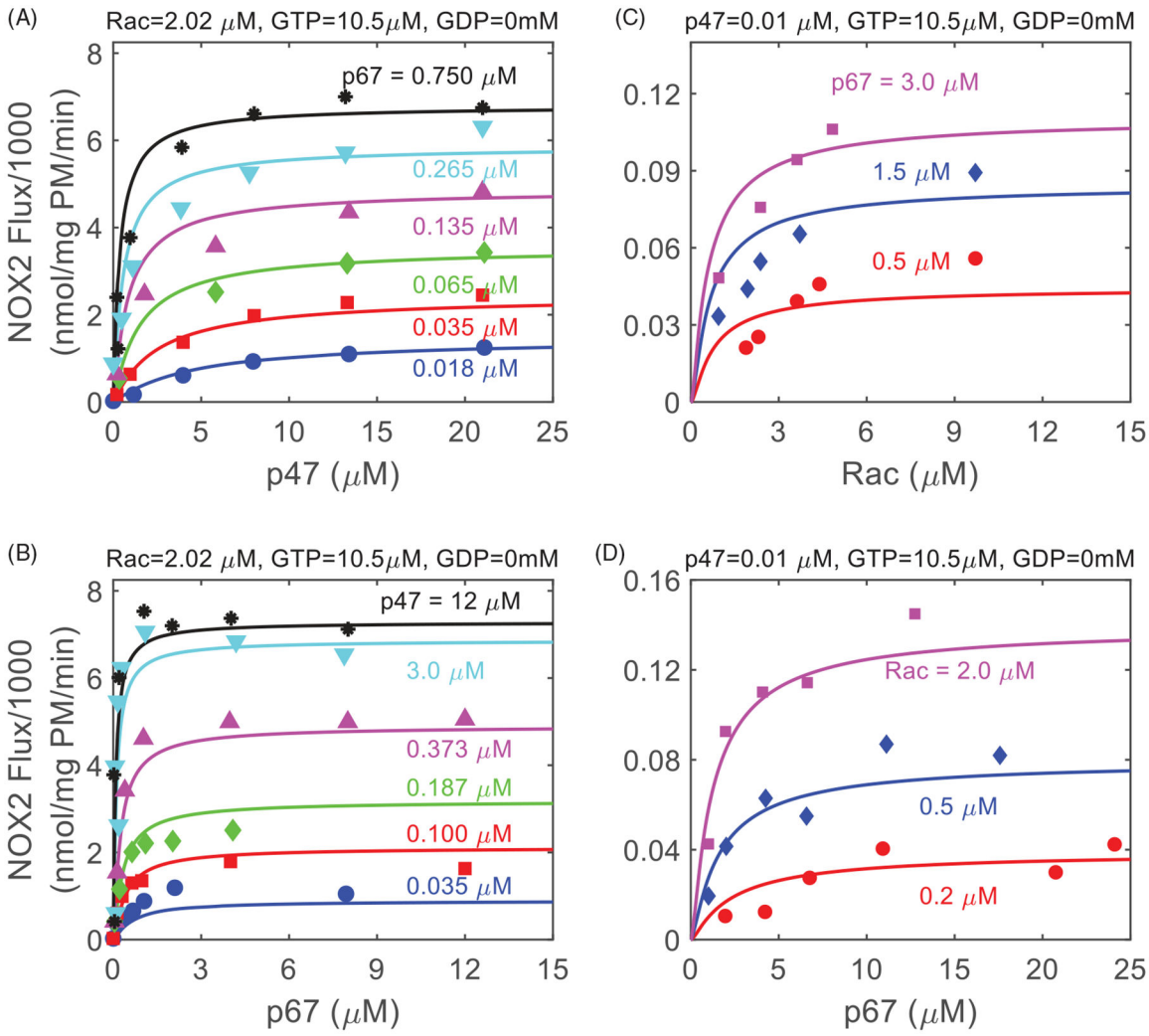

Figure 5.

Model fittings to the experimental data of Uhlinger et al. [61] and Nisimoto et al. [62] on the mutual enhancements of cytosolic subunits binding to the membrane subunits in cell-free systems. (A, B) Model simulations are compared to the experimental data of Uhlinger et al. [61] on the regulatory effects of the subunits p47^{phox} and p67^{phox} on each other's binding enhancement to the membrane subunits which in turn increases NOX2 activity (mutual binding enhancement). Specifically, the plots show the rates of $O_2^{\cdot -}$ production *via* the assembled and activated NOX2 complex as functions of varying concentrations of the cytosolic subunits p47^{phox} and p67^{phox}, with Rac concentration fixed at 2.02 μM in the presence of 10.5 μM GTP (absence of GDPβS). (C, D) Model simulations are compared to the experimental data of Nisimoto et al. [62] on the regulatory effects of the subunits Rac and p67^{phox} on each other's binding enhancement to the membrane subunits which in turn increases NOX2 activity (mutual binding enhancement). Specifically, the plots show the rates of $O_2^{\cdot -}$ production *via* the assembled and activated NOX2 complex as functions of varying concentrations of the cytosolic subunits p67^{phox} and Rac, with p47^{phox} concentration fixed at 0.01 μM in the presence of 10.5 μM GTPγS (absence of GDPβS).

Model-simulated lines for NOX2 flux as a function of Rac and $p67^{phox}$ are within ±10% of the reported values. In all experiments of Uhlinger et al. [61], 50 μl of reaction mixtures (pH = 7.4) contained 10 μg of plasma membrane (PM), or equivalently 8.6 pmol of Flavocytb_{558}, providing an appropriate concentration of total NOX2 complex for model simulations. All experiments of Nisimoto et al. [62] were performed at pH of 7.4 and 10 nM Cytb_{558}. In addition, the substrates NADPH and O_2 concentrations were very high (250 μM, saturated) in both Uhlinger at al. and Nisimoto *et al.* experiments. Model simulations are carried out using the estimated parameter values in Table 2.

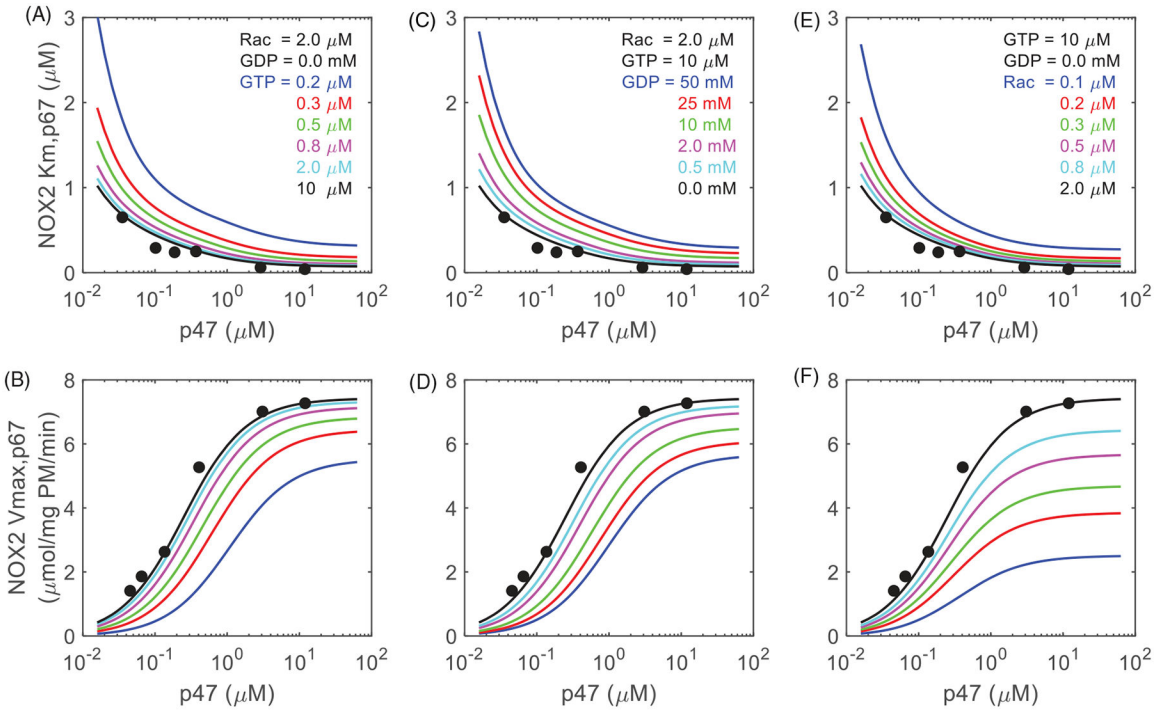

Figure 6.

Model predictions on the effects of varying concentrations of p47^{phox} on the kinetic parameters of NOX2 model for different concentrations of GTP, GDP, and Rac. Plots show model predictions on the effects of varying concentrations of the subunits p47^{phox} on the apparent K_m and V_{max} of p67^{phox} for (A, B) different concentrations of GTP with fixed GDP and Rac at 0 mM and 2 μM, respectively, (C, D) different concentrations of GDP with fixed GTP and Rac at 10 μM and 2 μM, respectively, and (E, F) different concentrations of Rac with fixed GTP and GDP at 10 μM and 0 mM, respectively. Plots also show the experimental data that were available from the Uhlinger *et al.* study [61] for GTP = 10 μM, GDP = 0 mM, and Rac = 2 μM. Experimental conditions used for model simulations are exactly the same as that described in Figures 5. Model predictions were carried out using the estimated parameter values in Table 2.

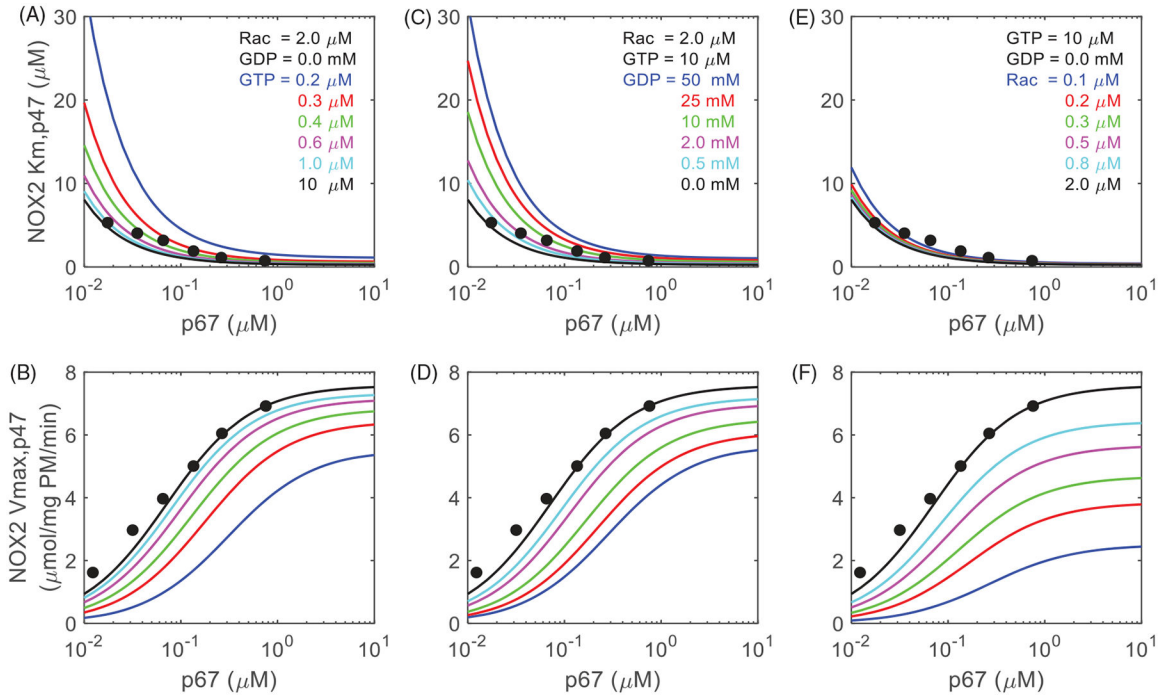

Figure 7.

Model predictions on the effects of varying concentrations of p67^{phox} on the kinetic parameters of NOX2 model for different concentrations of GTP, GDP, and Rac. Plots show model predictions on the effects of varying concentrations of the subunits p67^{phox} on the apparent K_m and V_{max} of p47^{phox} for (A, B) different concentrations of GTP with fixed GDP and Rac at 0 mM and 2 μM, respectively, (C, D) different concentrations of GDP with fixed GTP and Rac at 10 μM and 2 μM, respectively, (E, F) different concentrations of Rac with fixed GTP and GDP at 10 μM and 0 mM, respectively. Plots also show the experimental data that were available from the Uhlinger *et al.* study [61] for GTP = 10 μM, GDP = 0 mM, and Rac 2 μM. Experimental conditions used for model simulations are exactly the same as that described in Figure 5. Model predictions were carried out using the estimated parameter values in Table 2.

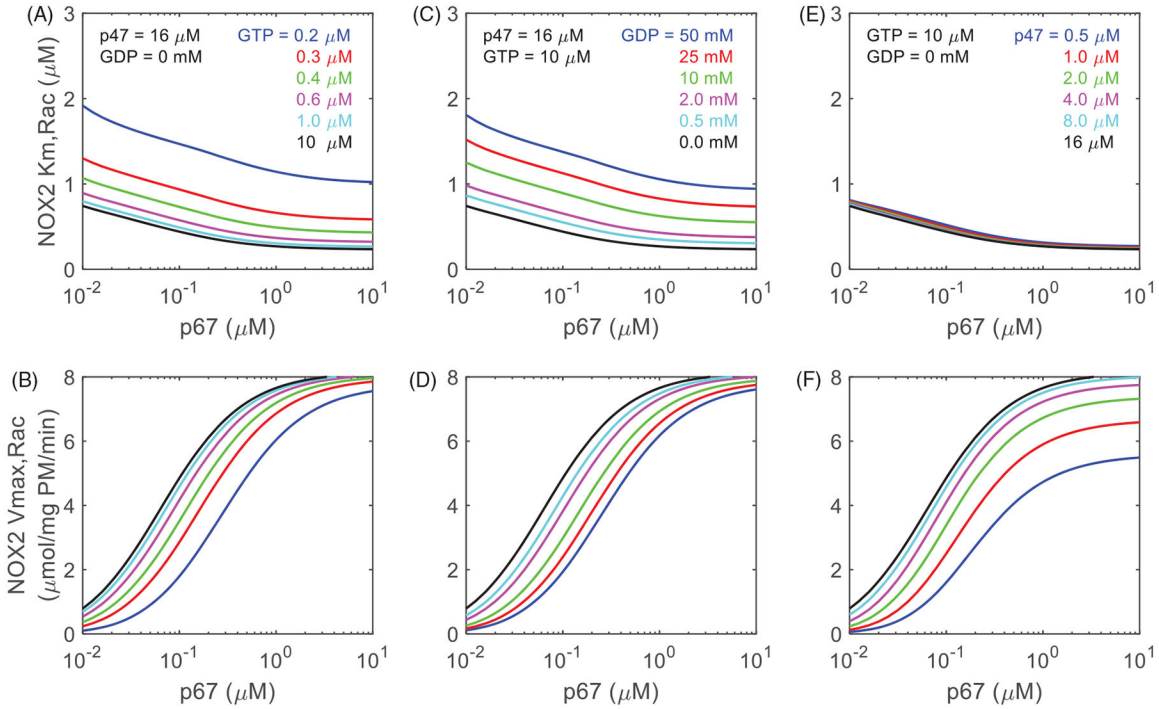

Figure 8.

Model predictions on the effects of varying concentrations of p67*phox* on the kinetic parameters of NOX2 model for different concentrations of GTP, GDP, and p47*phox*. Plots show model predictions on the effects of varying concentrations of the subunits p67*phox* on the apparent K_m and V_{max} of Rac for (A, B) different concentrations of GTP with fixed GDP and p47*phox* fixed at 0 mM and 16 μM, respectively, (C, D) different concentrations of GDP with fixed GTP and p47*phox* at 10 μM and 16 μM, respectively, and (E, F) different concentrations of p47*phox* with fixed GTP and GDP at 10 μM and 0 mM, respectively. Experimental conditions used for model simulations are exactly the same as that described in Figure 5. Model predictions were carried out using the estimated parameter values in Table 2.

Table 1.

Estimated parameter values for the model (Model 3 = Model 2 = Model 1) of NOX2 assembly and activation, fitted jointly to the experimental data of Cross et al. [63,64].

Parameter	Definition/Comments	Value	Units
C_{Etot}	Total NOX2 enzyme concentration (known from the experimental conditions)	Vary depending on the experiment/assay	μM
k_{NOX2}	NOX2 catalytic constant (Cross [64])	826.7	1/sec
k_{NOX2}	NOX2 catalytic constant (Cross et al. [63])	204.5	1/sec
$K'_{\mathrm{p47}} = K_{\mathrm{p47}}$	$p47^{phox}$ binding constant for the membrane subunits	0.029	μM
$K'_{\mathrm{p67}} = K_{\mathrm{p67}}$	$p67^{phox}$ binding constant for the membrane subunits	0.00038	μM
$K'_{\mathrm{Rac}} = K_{\mathrm{Rac}}$	Rac binding constant for the membrane subunits	0.00063	μM
K''_{p40}	$p40^{phox}$ regulatory constant for the p47 binding enhancement	0.005	μM

Table 2.

Estimated and fixed parameter values for Model 2 and Model 3 for NOX2 assembly and activation, fitted jointly to the experimental data of Uhlinger et al. [60,61], Peveri et al. [59], and Nisimoto et al. [62].

Parameter	Definition/Comments	Model 2 Values	Model 3 Values	Units
C_{Etot}	Total NOX2 enzyme concentration (known from the experimental conditions)	Vary depending on the experiment/assay	Vary depending on the experiment/assay	μM
k_{NOX2}	NOX2 catalytic constant	155	160	1/sec
K_{p47}	$p47^{phox}$ binding constant for the membrane subunits	0.21	0.24	μM
K_{p67}	$p67^{phox}$ binding constant for the membrane subunits	0.05 (fixed)	0.06	μM
K_{Rac}	Rac binding constant for the membrane subunits	0.20	0.22	μM
K''_{p67p47}	$p67^{phox}$ regulatory constant for enhancing the $p47^{phox}$ binding affinity	0.28 (K''_{p67})	0.30	μM
K''_{Racp47}	Rac regulatory constant for enhancing the $p47^{phox}$ binding affinity	0.11 (K''_{Rac})	0.05	μM
K''_{p47p67}	$p47^{phox}$ regulatory constant for enhancing the $p67^{phox}$ binding affinity	0.03 (K''_{p47})	0.11	μM
K''_{Racp67}	Rac regulatory constant for enhancing the $p67^{phox}$ binding affinity	0.11 (K''_{Rac})	0.33	μM
K''_{p47Rac}	$p47^{phox}$ regulatory constant for enhancing the Rac binding affinity	0.03 (K''_{p47})	0.009	μM
K''_{p67Rac}	$p67^{phox}$ regulatory constant for enhancing the Rac binding affinity	0.28 (K''_{p67})	0.003	μM
K_{GTP}	GTP regulatory constant for enhancing the $p47^{phox}$, $p67^{phox}$ and Rac binding affinities	0.41	0.36	μM
K_{GDP}	GDP regulatory constant for inhibiting the $p47^{phox}$, $p67^{phox}$ and Rac binding affinities	4387	5561	μM
Rac_b	Basal concentration of Rac (Uhlinger et al. [60])	0.02 (fixed)	0.02 (fixed)	μM
GTP_b	Basal concentration of GTP (Uhlinger et al. [60])	0.5 (fixed)	0.5 (fixed)	μM
$p47_b$	Basal concentration of $p47^{phox}$ (Nisimoto et al. [62])	0.01 (fixed)	0.01 (fixed)	μM
nT	Hill coefficient for the $p47^{phox}$, $p67^{phox}$ and Rac regulation by GTP	2.0 (fixed)	2.0 (fixed)	Unitless
nD	Hill coefficient for the $p47^{phox}$, $p67^{phox}$ and Rac regulation by GDP	0.5 (fixed)	0.5 (fixed)	Unitless
SSD	Sum of squared differences (least squared error)	5.85	3.01	Unitless
AIC	Akaike's information criterion	−581	−692	Unitless

The table also includes the computed values of SSD and AIC based on the estimated and fixed parameter values.

Free Radic Res. Author manuscript; available in PMC 2021 June 21.